

Temperature Effects in Polymer Electrolyte Membrane Fuel Cells

Tim Lochner^{+, [a, b]} Regina M. Kluge^{+, [a]} Johannes Fichtner^{+, [a]} Hany A. El-Sayed,^[c]
Batyar Garlyyev,^{*[a]} and Aliaksandr S. Bandarenka^{*[a, d]}



The behavior of proton exchange membrane fuel cells (PEMFCs) strongly depends on the operational temperatures. In mobile applications, for instance in fuel cell electric vehicles, PEMFC stacks are often subjected to temperatures as low as -20°C , especially during cold start periods, and to temperatures up to 120°C during regular operation. Therefore, it is important to understand the impact of temperature on the performance and degradation of hydrogen fuel cells to ensure a stable system operation. To get a comprehensive understanding of the

temperature effects in PEMFCs, this manuscript addresses and summarizes *in-situ* and *ex-situ* investigations of fuel cells operated at different temperatures. Initially, different measurement techniques for thermal monitoring are presented. Afterwards, the temperature effects related to the degradation and performance of main membrane electrode assembly components, namely gas diffusion layers, proton exchange membranes and catalyst layers, are analyzed.

1. Introduction

The European Union's environment and energy policy is strongly focused on moving away from fossil fuel towards renewable energy supply, in order to reduce greenhouse gas (GHG) emissions. In 2014, the global transport sector accounted for approximately 20% of overall GHG emissions. To decarbonize this sector, several European countries plan to stop the sale of vehicles based on internal combustion engines (ICEs) between 2025 and 2040. Several corresponding directives already came into effect. An alternative to conventional ICE driven cars are battery (BEV) and fuel cell electric vehicles (FCEVs). BEVs possess several advantages due to an increased well-to-wheel efficiency. Nonetheless, based on recent state-of-the-art technology, FCEVs show higher driving ranges, lower refueling time and an exhibit overall increased lifetime. Furthermore, hydrogen can act as an energy storage medium for intermittent periods of solar and wind energy production. Therefore, several automotive manufacturers like Honda, Hyundai and Toyota already started series production of FCEVs.^[1,2,3] Other companies like the BMW group announced to launch a test fleet of FCEVs in 2022.

To date, proton exchange membrane fuel cells (PEMFCs) are the most prominent types of fuel cells for automotive applications. The typical operating temperature of such PEMFCs ranges between 25 and 85°C . Heat removal of a thermal system

depends on both, its operational and the ambient temperatures. Therefore, especially in regions of higher temperatures, heat removal of a FCEV can be challenging. Albeit PEMFCs with operational temperatures up to 200°C could overcome these cooling issues, they are currently not considered for automotive applications, mainly due to limited power densities.^[4,5]

Furthermore, there is an increasing interest to operate PEMFCs at temperature near 120°C , because increased operational temperatures enhance the tolerance of the fuel cell towards CO poisoning, facilitate water management and increase the efficiency of the electrochemical reactions. The lower demand of cooling power in combination with an increase in electrochemical efficiency leads to a higher overall system efficiency. However, a main drawback of high temperature operation is the accelerated degradation of most fuel cell components, especially concerning the membrane electrode assembly (MEA). Hence, the trade-off between performance and lifetime needs to be carefully investigated.^[6,7]

Similarly, the lower temperature limit for FCEV operation is determined by the environmental conditions. Vehicles need to operate at sub-freezing temperatures, especially during cold start in respective climate zones. Low temperatures can lead to damage of the fuel cell components, in particular due to ice formation. Moreover, poor electrode kinetics limit the system performance when starting up the FCEV.^[6,8,9]

Herein, we highlight the effect of temperature on the performance and degradation of PEMFC components. We mainly focus on the low temperature hydrogen fuel cells, where special emphasis is put on the behavior of MEA components, namely the gas diffusion layer (GDL), the anode and cathode catalyst layers (ACL and CCL, respectively) and the proton exchange membrane (PEM). At first, *in-situ* and *ex-situ* monitoring techniques are addressed, which can be used to observe both overall and local temperature effects during PEMFC operation. Heterogeneity of the temperature distribution can help to gain insight into the local current densities and the relative humidification, which are, in turn, closely related to the performance of the fuel cell. The second part focusses on the temperature effects related to the materials present in the MEA due to its key function regarding PEMFC performance. Hereby, degradation at low and high temperature is compared, accompanied by promising mitigation strategies.


[a] T. Lochner,^{*} R. M. Kluge,^{*} J. Fichtner,^{*} Dr. B. Garlyyev, Prof. Dr. A. S. Bandarenka
Department of Physics, Physics of Energy Conversion and Storage
Technical University of Munich
James-Franck-Str. 1, 85748 Garching bei München, Germany
E-mail: batyr.garlyyev@tum.de
bandarenka@ph.tum.de

[b] T. Lochner^{*}
BMW Group
Taanusstr. 41, 80809 München, Germany

[c] Dr. H. A. El-Sayed
Department of Chemistry, Chair of Technical Electrochemistry
Technical University of Munich
Lichtenbergstraße 4, 85748 Garching bei München, Germany

[d] Prof. Dr. A. S. Bandarenka
Catalysis Research Center
Technical University of Munich
Ernst-Otto-Fischer-Str. 1, 85748 Garching bei München, Germany

[[†]] These authors contributed equally to this work

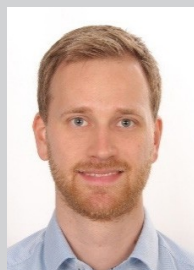
 © 2020 The Authors. Published by Wiley-VCH Verlag GmbH & Co. KGaA. This is an open access article under the terms of the Creative Commons Attribution License, which permits use, distribution and reproduction in any medium, provided the original work is properly cited. Open access funding enabled and organized by Projekt DEAL.

2. Monitoring Techniques

The local temperature of a PEMFC has an effect on parameters such as current density and reaction kinetics, kinetics of degradation processes, water drag, back diffusion and proton conductivity of the membrane.^[10] Therefore, monitoring the temperature during fuel cell operation is an effective tool to validate fuel cell design parameters, operational strategies (e.g. cold start, start-up, shut-down) and fuel cell materials. In the following, widely used and promising techniques for *in-* and *ex-situ* monitoring of the cell temperature will be reported and discussed.

2.1. *In-situ* Monitoring

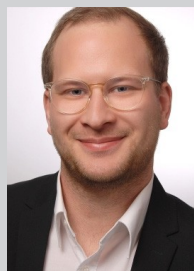
The position of the temperature sensor in the fuel cell is optional and depends on the desired technique and the system. Possible sensor locations include the membrane, catalyst layers or gas diffusion layers, as well as at the interfaces between them. In general, temperature gradients can be measured parallel to the flow field channels or perpendicular to the membrane. The following section focuses on *in-situ* techniques such as infrared cameras, lock-in thermography, electro-thermal impedance spectroscopy, thermocouples and optical methods, as well as their prospects in understanding the working principle of the fuel cells relative to the temperature.



Tim Lochner received his Master's degree from the Technical University of Denmark in 2016. His Master's thesis dealt with degradation effects in proton exchange membrane fuel cells. He was working for 2 years on fuel cells for domestic heating applications at the Elcore GmbH. In 2018, he started his PhD in cooperation with the BMW Group and the Technical University of Munich (Germany) under supervision of Prof. Dr. Bandarenka. His PhD research deals with impedance based on-road monitoring of fuel cells for automotive applications.



Regina M. Kluge is a PhD candidate at the chair for Energy Conversion and Storage at the Technical University of Munich. She received her Master in Condensed Matter Physics at the same university in 2017, where she was concentrating on functional materials for energy conversion, more precisely organic thermoelectric materials. Since she never lost her interest in the central topic of energy, her current research is focusing on the determination of electrocatalytically active sites via electrochemical scanning tunneling microscopy.



Johannes Fichtner received his BSc and MSc in Molecular Nano Science from the University of Erlangen-Nuremberg (Germany) in 2015 and 2017, respectively. Since 2017, he conducts his PhD studies in the group of Prof. Bandarenka at the Technical University of Munich (Germany). His research interests include the (top-down) synthesis and characterization of functional energy materials such as nanostructured Pt (alloys) for the oxygen reduction reaction catalysis in PEM fuel cells.



Hany A. El-Sayed is a research associate at the chair of technical electrochemistry at Technical University of Munich (Germany). Leading a small group of PhD students in the research group of Prof. Hubert Gasteiger, El-Sayed's research efforts focus on the development of novel catalysts for proton exchange membrane fuel cells and electrolyzers. El-Sayed received his PhD in physical chemistry in 2011



from the University of Calgary (Canada), where he performed research under the supervision of Prof. Viola Birss in the area of electrochemical materials science. His PhD research work included the development of nano-templates using electrochemical approaches and using them for nano-electrode array formation.

Batyr Garlyyev received MSc degree from Georgia Institute of Technology (Atlanta, USA) in 2013 and PhD degree from the same institute in 2016, where he worked on synthesis of nanostructured materials with Prof. Dr. Mostafa El-Sayed. Thereafter, he started his postdoctoral research in the group of Prof. Dr. Bandarenka at Technical University of Munich (Germany). His research focuses on electrocatalysis for green energy conversion technologies. In summer of 2016, Dr. Garlyyev was awarded TUM University Foundation Fellowship.



Aliaksandr S. Bandarenka received his PhD from Belarusian State University in 2005. After a postdoc at the University of Twente (Netherlands) and Technical University of Denmark, he joined the Center for Electrochemical Sciences (CES) at Ruhr University Bochum (Germany) as a group leader (2010–2014). Currently, he is an Associate Professor at the Department of Physics, Technical University of Munich (Germany). His research interests focus on the development of electrocatalysts, methodologies for characterization and modification of electrified solid/liquid interfaces, and interfacial charge transfer.

The use of infrared cameras is one of the most popular applications to monitor the temperature distribution along the flow field channels of a fuel cell. A schematic of the setup is depicted in Figure 1a. The technique requires the implementation of infrared transmitting materials, e.g. as bipolar plate (BPP) material. These windows are usually based on different materials such as zinc selenide,^[11] barium fluoride,^[12] calcium fluoride^[13] or sapphire.^[14] It is important to mention, that most infrared transparent materials have lower thermal and electrical conductivities compared to graphite and stainless steel. For instance, the thermal conductivity of zinc selenide is in the order of one tenth compared to that of graphite.^[15,16] Therefore, temperature gradients might be increased when using aforementioned infrared transmitting materials. This effect is especially pronounced when the local current density and cooling performance are unevenly distributed.

An infrared camera records thermal images of the selected electrode and flow field channels during the operation of the cell. The infrared camera can monitor heterogeneities in the temperature distribution, which can be exploited to gain insight into the operation processes of a single MEA. In regions of high currents, the reaction enthalpy is increased, which in turn leads to an increase in the temperature.^[11,12,14] Moreover, by using infrared and visible light transmitting materials, liquid water droplets can be observed simultaneously with temperature

distributions. Hereby, the less flooded the areas within the cell, the more homogeneous the temperature distribution. This is especially dominant when operating at high stoichiometries.^[11] Additionally, the humidification of the reactant gases can significantly impact the temperature distribution. Low hydrogen humidification leads to higher ohmic overpotentials from anode inlet towards outlet, inducing high temperatures at the anode outlet. Due to the oxygen partial pressure, the current density at the cathode inlet is higher than at the cathode outlet. Therefore, a counter-flow configuration is suggested to balance kinetic and ohmic overpotentials reaching a homogeneous temperature distribution within the cell.^[14] Moreover, gravitational effects can impact the temperature distribution due to water droplet formation. Cathode flow field channels facing upwards can induce evaporation of water droplets. This effect might be most relevant for open-cathode fuel cells.^[17] In order to optimize thermal management, the media flow rates need to be chosen carefully. The flow rate of hydrogen and the temperature distribution can differ in different channels of the flow field. In channels with lower gas flow rates, the temperature is typically reduced. This is a direct result of increased current densities in regions with higher supply of reactants. It can be concluded that a homogeneous gas distribution is incremental to reach uniform temperature profiles along the active area. Therefore, the MEA surface temperature at the

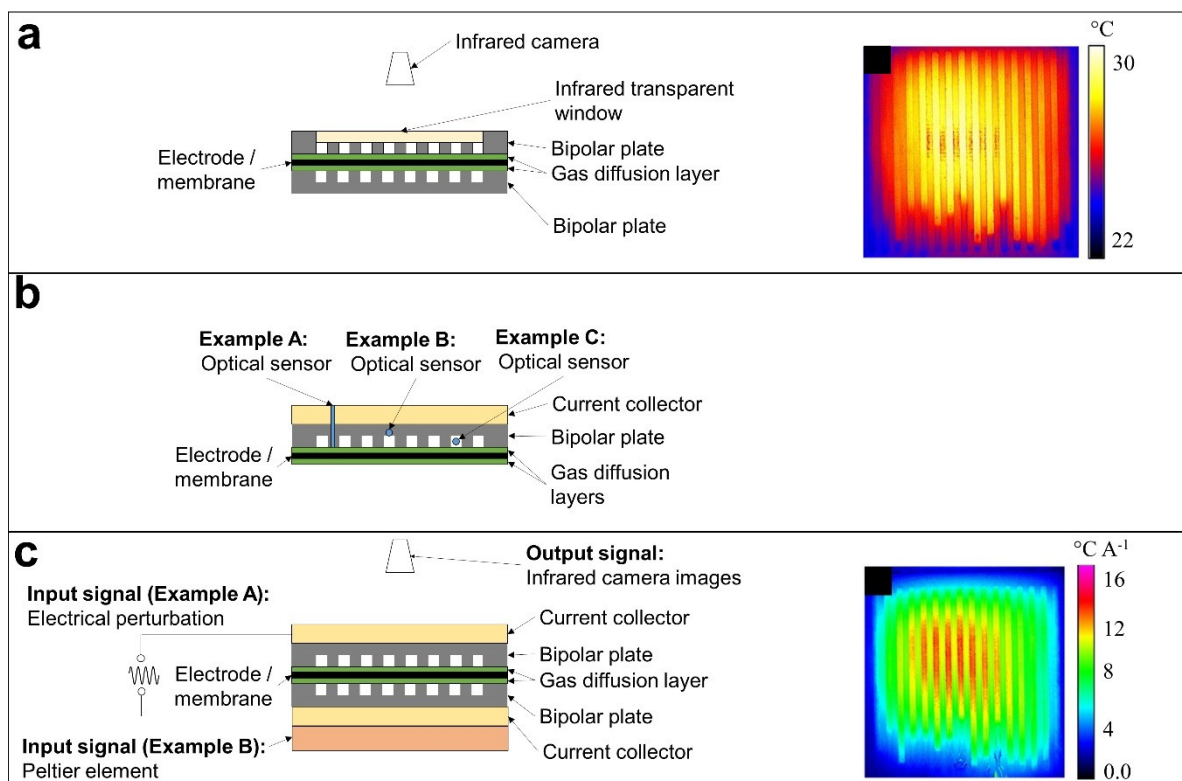


Figure 1. Schematic illustration (left) of different types of temperature distribution measurements. a) Schematic of a temperature distribution measurement setup using an infrared camera to monitor the surface of the GDL and the gas flow channels of an arbitrary electrode. b) Temperature measurement using optical methodologies. The examples describe two types of sensor placements that can be either perpendicular (Example A) or parallel (Examples B and C) to the membrane. c) Measurement principle of electro-thermal impedance spectroscopy. Here, the input signal is periodically modulated heat that can be induced by e.g. modulation of the electrical current (Example A) or by a Peltier element (Example B). The right images show representative measurements on lab scale fuel cells.^[22] Copyright 2016 Elsevier.

media inlet is decreased due to convective heat transport between the reactant gases and the GDL.^[18]

As described above, several mechanisms lead to inhomogeneous temperature distributions within a single MEA. Therefore, when operating a fuel cell stack, it is expected to have differences in temperature between the cells. In a recent study,^[19] using infrared imaging techniques, temperature differences up to 12 °C were measured along an air-cooled stack. The highest temperature difference is typically monitored between the active and the cooling channel. Within a single MEA, a temperature gradient of 2.5 °C was observed. This impacts the performance of every individual MEA within a stack, as well as the specific areas within an individual MEA. Hence, the variation of the performance is increased at low operating temperatures and high current densities.

Besides affecting the performance of a fuel cell stack, the temperature also impacts the degradation of the different fuel cell components. Infrared cameras are used to detect pinholes within the membrane, leading to gas crossover between anode and cathode. The exothermal reaction of hydrogen and oxygen at the platinum surface of the CCL can cause pinholes which can be detected by the infrared camera.^[20] However, condensation of water within the flow field channels interferes with the measurement of the GDL surface temperature when using infrared imaging techniques. Despite the prospects of infrared imaging at elevated temperatures, their sensitivity is limited towards the changes at low temperatures. Furthermore, water generation inhibits thermal imaging of the electrode surface, which is especially critical when observing the cathode.^[21] In addition, differences in emissivity of the fuel cell materials interfere with the infrared imaging and remain a major challenge.^[22] Infrared imaging might also change the performance of the fuel cell and the transparent window can act as a heat sink and, therefore, affect the PEMFC operation.^[18]

Therefore, lock-in thermography is a technique that enhances the detection limits of traditional infrared imaging to below 100 μK and overcomes several limitations of classical thermal imaging.^[23] The methodology gives information on local heat sources, material defects, thermal impedances and thermal capacitances and is mainly applied for temperature distributions within the flow field plane. Since no adoption of the cell setup is required, it is a potential operando measurement technique. When modulating the introduced heat with different frequencies, the method is sometimes referred to as electrothermal impedance spectroscopy (ETIS). The principle of ETIS is illustrated in Figure 1c. For that reason, periodically modulated heat is introduced to the fuel cell. This can, for example, be achieved by modulation of the electrical current (Figure 1c, Example A) or directly inducing heat modulations by using a Peltier element (Figure 1c, Example B). An infrared camera periodically monitors the surface temperature change of the cell. The signal is further processed using, e.g. lock-in thermography techniques that are able to compare the amplitude and phase delay of the output to the input signal. Lock-in thermography thereby reduces the noise of the infrared camera.^[22] The data can be analyzed in a similar way to electrochemical impedance spectroscopy (EIS).^[24] Here, the

amplitude is the ratio of the peak amplitude of the thermal response and the current perturbation. The larger the amplitude, the higher is the thermal impedance of the cell. The phase shift between thermal response and current perturbation indicates the thermal capacitance of the cell. This technique allows the detection of cracks and defects within the cell due to their different thermal behavior. Moreover, liquid water formation can be observed.^[22,25]

Compared to classical thermal imaging, ETIS is not able to detect pinholes within the polymer membrane since corresponding images only represent processes that are driven by changes in current (e.g. water formation). The advantages of ETIS is its insensitivity to lens reflections and insensitivity to thermal emissivity of different fuel cell materials. Since ETIS does not rely on the use of infrared transmitting materials it has a very low interference with the system under observation. ETIS is capable of identifying water droplets even when generated under the BPP land areas.^[22]

EIS is a methodology that can be used for monitoring of fuel cell systems, especially with respect to sub-zero operation.^[26] EIS during system operation does currently not allow a localized temperature analysis such as aforementioned imaging techniques. Nevertheless, the impedance based high frequency resistance can be attributed to water content within the polymer membrane and is therefore a relevant parameter for operational strategies to start up automotive fuel cells.^[27,28] A more comprehensive overview on cold starts of PEMFCs is provided elsewhere.^[29]

An alternative to aforementioned methods is the insertion of thermocouples between the different layers and interfaces of the fuel cell, in order to measure local temperatures. This technique is capable of measuring the temperature distributions along the flow field channel direction, as well as perpendicular to the membrane. In order to apply this technique, the setup of the fuel cell has to be redesigned, e.g. concerning the gas transport. The usage of thermocouples results in complementary observations to infrared imaging,^[11,14] e.g. an increase in anode temperature due to water condensation. In an early application of this method, the thermocouple was placed perpendicular to the membrane on the BPP/ GDL and catalyst layer/ membrane interfaces of cathode and anode. Hereby, it was not only possible to locally monitor the temperature, but also to measure the thermal conductivity ($0.2 \text{ W m}^{-1} \text{ K}^{-1}$) of the catalyst layer surface and GDL.^[30] Degradation of fuel cells often occurs due to flooding of the anode or cathode compartments. Water condensation is likely to happen at the interface between GDL and BPP.³¹ In order to avoid flooding, it is important to optimize the surface of BPPs to minimize droplet formation and to enhance proper liquid water removal.

As a fourth option, optical sensors can be used to measure temperature distributions on the GDL surface along the flow field channels. Here, an optical fiber is inserted into the PEMFC. In order to gain access to the internal PEMFC components, it is often necessary to mill out parts of the surrounding fuel cell setup (e.g. BPP or end plate). Consequently, this requires a modified setup. Exemplary setups are shown in Figure 1b. In Example A, the current collector and end plate are milled out

and a sensor (e.g. optical fiber) is inserted. In Example B, only the BPP is milled out to the corner of the cell. Both setups allow simultaneous fuel cell operation and temperature measurements.

In the following, two optical methodologies are introduced, namely tunable diode laser absorption spectroscopy and in-fiber Bragg gratings. Tunable diode laser absorption spectroscopy can be used to simultaneously determine the average temperature and humidity of two flow field channels. Accuracies of $\pm 5\%$ of water partial pressure and ± 2 K for temperature measurements are recorded in literature.^[32] The laser beam is directed into the gas phase of two flow field channels of the cathode. Results using this technique show a more homogeneous relative humidity along the flow field when the overall cell temperature is increased. It is assumed that at high cell temperatures the main contributor to the overall water transport mainly originates from advection of water.^[32] At low cell temperatures, electro-osmotic drag via the membrane dominates the water distribution. Therefore, relative humidity builds up from cathode inlet towards outlet due to water production from the electrochemical reaction. During load cycling of the cell it could be shown that the partial pressure of water closely follows the current density. Nevertheless, the temperature lags behind the load cycles due to the larger thermal inertia of the cell.^[32]

In-fiber Bragg gratings are another methodology used for optical sensors to monitor the temperature distribution within PEMFCs. The methodology is also capable of measuring the local relative humidity with an accuracy of $\pm 2\%$.^[33] This measurement type has a higher temperature accuracy of ± 0.2 K compared to the tunable laser absorption spectroscopy approach (accuracy: ± 2 K).^[30,34] The technique allows to correlate performance and humidity and identify hysteresis effects during polarization curve measurements. When ramping the load current of the PEMFC down, the performance and relative humidity are increased.^[33]

The optical methodologies described earlier show limited spatial resolution since the sensors measure average temperatures along the flow field channel path of 1 to 5 cm. To overcome this limitation, measurement setups similar to Example A in Figure 1b can be used.^[35,36] The sensor principle can be based on the "lifetime-decay method" of phosphor to determine the local GDL temperature. The optical sensor is thereby mounted perpendicular to the GDL. On top of the GDL, chromium doped $Y_3Al_5O_{12}$ is used as a luminescent material. Five sensors are positioned on the cathode GDL from the air inlet towards the outlet. A temperature deviation of $\pm 5\%$ could be obtained. It is found that the cell temperature at high inlet relative humidity and low current densities becomes unstable due to poor water and heat removal. This is in good agreement with findings from infrared thermal imaging.^[11] Despite literature reports claiming that the cell temperature lags behind the load current due to the large thermal inertia of the cell,^[12,30] it was found that the GDL surface temperature quickly follows the load current due to its low thermal inertia. The different findings might originate from the location of the sensors. An increased time shift between temperature and load current is

found when measuring at the surface of the cell setup,^[12] while low time shifts are observed when measuring within the gas phase of the media supply.^[30]

In summary, the three presented temperature-monitoring techniques (Figure 1) are suitable to solve different scientific problems. In terms of resolution, one needs to classify three categories – time, spatial and temperature resolution. Optical sensors typically show low spatial resolution, compared to 0.3 mm and 78 μm for thermal and electro-thermal imaging, respectively.^[18,22] Since the spatial resolution of ETIS increases with measurement time, its time resolution is limited.^[37] In contrast, classical thermal imaging and the use of optical sensors allows temperature distribution monitoring in real-time. ETIS can achieve high temperature resolutions in the range of 5 to 20 μK (1000 s measurement time), compared to 20 mK using thermal imaging and 200 mK using optical sensors.^[23,19,33]

2.2. Ex-situ Analysis

In-situ investigations correlate local operating parameters such as temperature, humidity and current density to local performance degradation rates. *Ex-situ* investigations complement *in-situ* measurements; they help to understand the mechanisms that lead to degradation.

In this regard, post-mortem analysis of fuel cell components after operation at different temperatures is a facile way to get insights into internal degradation of the cell. The following section gives an overview on these investigations by categorizing three temperature ranges: operation below 0 °C, 40–100 °C and above 100 °C. A significant focus is given to the degradation of BPPs, GDLs, microporous layers (MPLs), electrodes and the membrane.

PEMFC degradation below 0 °C is especially relevant in transport applications when the system needs to start-up at subzero temperatures. The phase transition of liquid water to ice within the porous layers (e.g. CL, MPL, GDL) and between the different fuel cell layers can cause mechanical damage of the cell components.^[38] Water within the pores of the electrodes stays in a super-cooled state, as long as the water droplet does not reach a critical cluster diameter. This critical diameter is strongly dependent on the properties of the porous material, such as hydrophobicity, as well as on temperature. In general, one can state that freezing of water is suppressed within the GDL/ MPL pores when hydrophobicity is increased, pore size is decreased, and temperature is increased.^[39]

Start-ups below -5 °C show irreversible performance losses that could be referred to mechanical failures such as CL delamination, cracks and pinholes in the membrane and a damage of the backing layer polymer coating. It can be assumed that membrane damages due to the freezing of water do not occur inside the membrane but at the interface between membrane and catalyst layer. Scanning electron microscopy (SEM) images show an increased roughness of the membrane surface, supporting this assumption.^[38] Water freezing inside pores can lead to mechanical damage due to an increase in volume when the water changes from liquid to ice. The severe

morphology change of the GDL as well as delamination of the layers seen in SEM images support this hypothesis.^[38] These mechanical failures can induce operational failure mechanisms due to media starvation of the electrodes.^[40] When cycling the MEA between -40 and 0.5 °C, water drains out of the membrane into the electrode layers. Consequently, water is freezing within the electrode layer causing increased porosity and decreased electrochemical active surface area (ECSA). This mechanism is more severe when the stack is shut down in wet conditions.^[34] Another material failure observed by SEM is cracking of the GDL fibers and delamination of the fuel cell layers. Nevertheless, these findings are not reproducible in all freeze start experiments. Compression of the fuel cell might prevent cracks within the GDL fibers. This is a possible explanation for different results found within literature due to different compression forces.^[34,38] SEM imaging shows that mainly the cathode electrode is affected by freeze/ thaw cycling, exhibiting an increased porosity and a decreased electrode surface area.^[34]

Hydrophobicity of the MPL plays an important role during cold-starts. As the main task of the MPL is water management, it determines if ice formation at the interfaces of the fuel cell layers (e.g. GDL/BPP) takes place.^[40] One function of the MPL during freeze start is to keep water in a super-cooled state and thereby, prevent freezing of droplets within the fuel cell layers. As discussed, ice can be found in different layers of the cell, such as the flow fields, GDL, MPL and CL, as well as at the interfaces between those and the membrane. The origin of ice formation and movement of ice during cold starts can be analyzed using cryo-SEM.^[41] At the beginning of the cold start, an ice layer is built inside the CCL in the proximity of the membrane. With increasing time, the region containing ice extends towards the MPL. This process depends on the current drawn during start-up. In case of low current densities (e.g. 0.01 A cm^{-2}), the ice containing region within the catalyst layer grows homogeneously between membrane and MPL. During a start-up at low current density, a large fraction of the CCL pores are filled with ice. In contrast, when the cold start is performed at increased current densities (e.g. 0.08 A cm^{-2}), vacant pores within the CL remain close to the membrane. This indicates that the amount of ice accumulated in the CL decreases with increasing start-up current.

One way to prevent mechanical damage of the fuel cell layers is the avoidance of ice formation by keeping water in a super-cooled state. The occurrence of super-cooled water is enhanced when using more hydrophobic materials. Another way of protecting the fuel cell layers during cold starts is the introduction of hydrophilic layers. Under high humidity and cold start conditions, the hydrophilic interlayer removes liquid water from other layers and thereby avoids blockage of gas diffusion from the BPP towards the CL. In dry operation modes, the hydrophilic layer is able to retain water inside the cell to inhibit dehydration.^[42] It is assumed that the layer removes liquid water during start-up from the cathode catalyst layer and thereby, avoids freezing of water within the cathode. Therefore, higher current densities during cold start-up can be reached, leading to an increase in cell temperature and hence, delays the

freezing of the generated water product.^[42] Some studies confirm that a hydrophilic MPL has the ability to suppress the formation of an ice layer.^[43] In contrast, the hydrophobic MPL material forms an ice layer at the interface of the catalyst/ MPL, while little water stays inside the layers, as shown in Figure 2.

No detailed literature on the impact of cold starts on BPP degradation was found to date. Nevertheless, post-mortem analysis of cold start effects on coated metallic BPPs might be beneficial, since different thermal expansion coefficients – especially for carbon coated BPPs^[44] – might also induce fuel cell failure.

It is well known that electrode degradation is increased (from 40 to 80 °C) under fully humidified conditions.^[45,46] Additionally, the pore size of the electrodes after operation increases when operating at higher temperatures. This implies higher carbon corrosion rates at higher temperatures. Also, the kinetic performance losses (based on electrochemical techniques) rise at higher temperatures. Modeling studies show that activation overpotentials due to Pt degradation explain the performance loss at 40 and 60 °C. However, the model underestimates the performance losses measured at 80 °C cell temperature. This indicates that at 80 °C, in addition to catalyst degradation, also membrane degradation takes place.^[46] Pt bands due to dissolution of Pt at the cathode are found within the membrane close to the CCL. The theoretical equations to determine the location of the Pt band can be well reproduced experimentally when including temperature dependences of the membrane permeability.^[47,46] In general, the location of the band depends on the crossover rates of oxygen and hydrogen through the membrane. The oxygen permeability of the membrane rises with increasing membrane temperature relative to the hydrogen permeability. Therefore, the band moves closer to the anode with increasing temperature.^[46] Furthermore, with increasing temperature, higher amounts of Pt can be found in the membrane.^[45,46]

The membrane performance can decrease due to chemical degradation and pinhole/crack formation.^[20,45] The influence of temperature on membrane behavior will be discussed in more detail in Section 3.3.

Metal BPP degradation can also depend on temperature. Especially degradation of the anode BPP depends on the local temperature, while degradation of the cathode BPP is correlated to local relative humidity.^[20] So far, no physical explanation of these observation could be found. The presence of

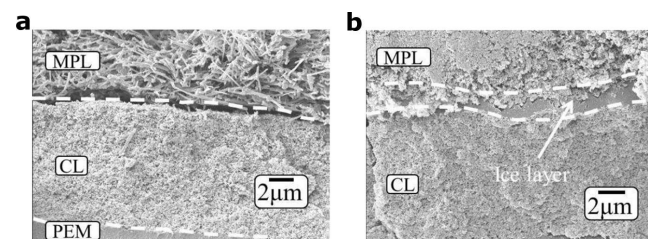


Figure 2. Cryo-SEM images of the cross-section of an MEA recorded after cold start operation. a) MPL/ CL interface, using a hydrophilic MPL material. b) MPL/ CL interface using a hydrophobic MPL material.^[43] Copyright 2018 IOP Publishing.

liquid water enhances corrosion of the cathode BPP, while evaporation of water in hot zones causes an increasing rate of deposits at the BPP surface.^[20] Hence, fluctuating local temperature at the BPP accelerates cathode BPP corrosion due to an increased frequency of condensation and evaporation.

Up to date, there is no detailed literature explaining the impact of cold starts on BPP degradation. Nevertheless, post-mortem analysis of cold start effects on coated metallic BPPs might be beneficial, since different thermal expansion coefficients – especially for carbon coated BPPs^[44] – might also induce fuel cell failure.

3. Influence of Temperature on the Degradation of the Membrane Electrode Assembly

3.1. Stability of the Catalyst Layers

During PEMFC operation, degradation of the cathode and anode catalyst layers majorly contributes to voltage losses observed in the cell. Typically, carbon supported Pt nanoparticles (Pt/C) are used as the active material in both electrodes. However, catalysis of the oxygen reduction reaction (ORR) at the cathode side using Pt/C-type catalysts is highly sensitive to the cell conditions, such as electrode potential sweep, pH, relative humidity or temperature. As summarized by Meier *et al.*,^[48] typical degradation mechanism of Pt/C include the dissolution, agglomeration, detachment and Ostwald ripening of the Pt nanoparticles, as well as support corrosion (Figure 3a). Accordingly, the impact of temperature on the degradation of Pt and its alloys will be reviewed in this section.

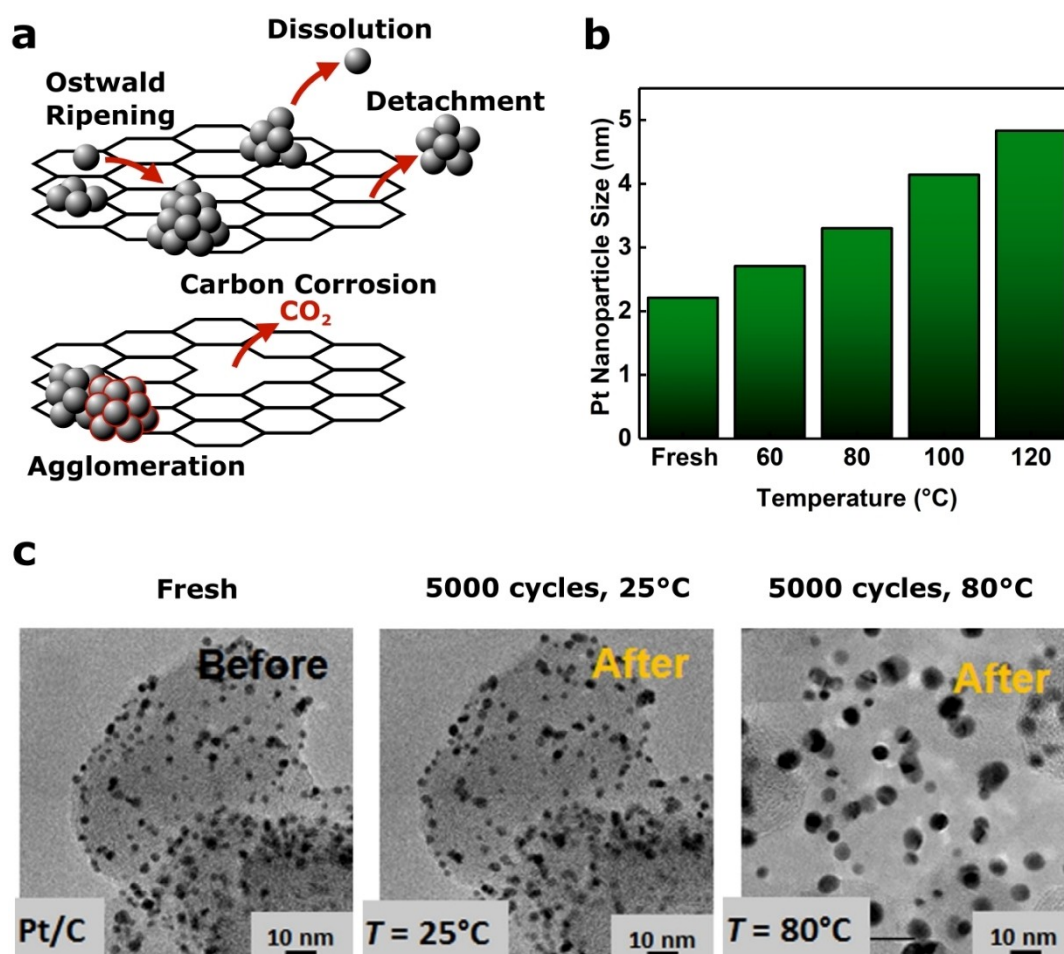


Figure 3. a) Schematic description of different degradation mechanisms typically occurring during voltage cycling of Pt/C, as proposed by Meier *et al.*^[48] b) Change of the Pt nanoparticle size during voltage cycling (0.1–0.96 V) with increasing cell temperature. The data values were obtained and replotted from Ref. [49] c) Excerpt of TEM images of fresh Pt/C, as well as after 5000 AST cycles between 0.6 and 1.05 V vs RHE in 0.1 M H₂SO₄ at 25 °C and 80 °C, respectively. Only minor changes can be observed at 25 °C, while the temperature increase strongly influences the morphology of Pt/C. Adapted with permission from Ref. [50] Copyright 2015 Elsevier.

In general, early catalyst durability studies indicate that temperature has a dominant role on the nanoparticle growth rate during voltage cycling, as depicted in Figure 3b.^[49] Similarly, studies by Bi *et al.* report strong particle growth during 7000 potential cycles between 0.87 and 1.2 V vs RHE, depending on the temperature.^[45] However, the ECSA losses of > 50% at 40 °C and > 75% at 80 °C can not only be traced back to increasing nanoparticle size. In fact, enhanced Pt mass loss also contributes to the ECSA loss, which is likely to be caused by Pt dissolution and particle detachment. In detail, ~25% loss was observed after cycling at 40 °C, compared to ~50% at 80 °C. This is further verified by Pt detected in the membrane, formed through reduction of Pt ions by crossover hydrogen.

Recent transmission electron microscopy (TEM) studies on the degradation of Pt/C during accelerated stress tests (ASTs) performed at different temperatures (conditions: 5000 cycles, 0.6–1.05 V vs RHE, 0.1 M H₂SO₄) further confirm the aforementioned relation.^[50] In detail, only minor morphological changes were observed at a cycling temperature of 25 °C, majorly assigned to the Pt re-deposition onto larger particles (Figure 3c). At elevated temperatures, not only the particle growth was strongly pronounced, but also severe reduction of small,

isolated particles and, in turn, a strong decrease of the ECSA was observed. Interestingly, at 80 °C, the morphological changes of the Pt nanoparticles during AST in liquid electrolyte are well comparable to catalyst degradation observed in a MEA under similar conditions.

Another important component determining the overall durability of a PEMFC is the catalyst support material. Corrosion of the carbon support, which is primarily correlated with the cell potential, also strongly contributes to overall CL degradation. In general, the carbon support undergoes oxidation into CO₂, leading to particle detachment, accelerated sintering of the Pt catalyst and, in turn, decrease in ECSA.^[51,52,53] As a consequence, large losses in the PEMFC performance are observed. The degree of the carbon degradation is shown to primarily depend on the morphology of the support. For instance, utilization of carbon nanofibers resulted in higher durability in comparison to carbon nanotubes and commercial carbon support materials during thermal corrosion tests, shown in Figure 4a.^[54] Interestingly, when no Pt catalyst is loaded onto the support, the degradation of the support is minimal and only ~1% weight loss is observed. However, in the presence of Pt, the weight loss is significantly increased, indicating that the

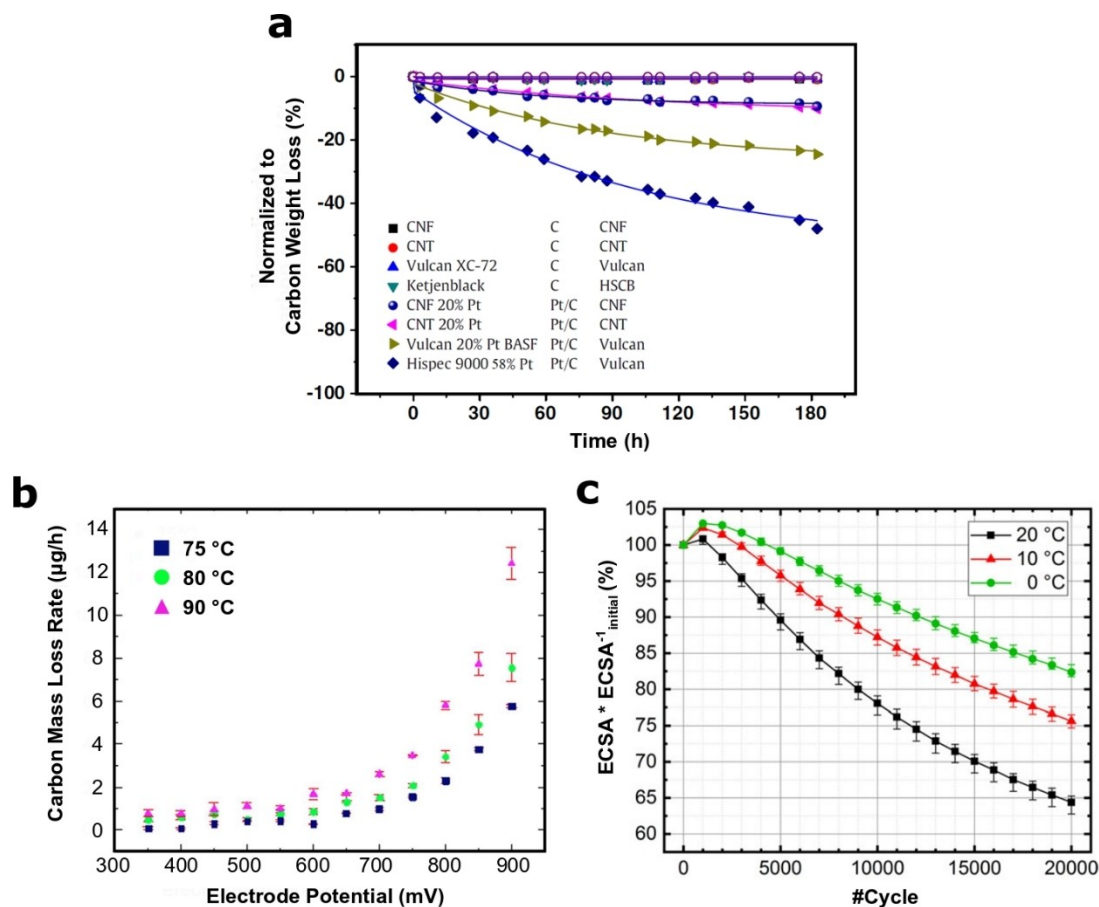


Figure 4. a) Weight loss of various carbon support materials at 200 °C with and without loaded Pt catalyst. The legends indicate the name, Pt loading and type of the support material. The figure is adapted with permission from Ref. [54] Copyright 2013 Elsevier. b) Loss of carbon mass plotted against the cell potential under potentiostatic conditions as function of cell temperature. Adapted with permission from Ref. [55] Copyright 2018 Electrochemical Society. c) Influence of substrate degradation measurements on the catalyst ECSA. Adapted with permission from Ref. [56] Copyright 2019 Wiley-VCH.

carbon corrosion is catalyzed by Pt. Furthermore, when the Pt loading is increased from 20% to 58%, the weight loss due to carbon corrosion is nearly doubled for Vulcan-type support materials. Additionally, presence of alloyed PtRu catalysts on carbon support (commonly at the anode side) resulted in higher degradation than pure Pt.^[54] The best thermal durability performance at 200°C was shown by the carbon fiber and nanotubes, resulting in less than 10% weight loss over 180 h period.

At temperatures closer to the operating temperature of a PEMFC, the degree of the support oxidation is shown against the cell potential in Figure 4b.^[55] As it is seen in the Figure, both the higher cell potential and the temperature contribute to accelerated oxidation of carbon support. Moreover, by decreasing the cell temperature closer to the freezing point of water, higher durability of the support is reported in literature (Figure 4c).^[56] The loss in the catalyst ECSA due to carbon corrosion is lower at 0°C, mainly due to the suppressed kinetics of carbon oxidation to CO/CO₂. With slight increase in the temperature to 20°C, the loss in ECSA is already significantly increased (Figure 4c).

Mitigation for the support corrosion can be achieved by using doped carbon substrates or alternative support materials. For instance, nitrogen-doped^[57] and boron-doped^[58] materials have shown to mitigate the carbon degradation. In addition to carbon-based support materials, TiO₂-based substrates were also suggested as a promising alternative.^[59] However, temperature-dependent durability of such support materials still needs to be investigated.

Nanostructured Pt_xM/C-type alloys are another important class of low-temperature PEMFC catalysts, which is mainly owed to their improved ORR kinetics compared to pure Pt/C. For instance, Pt_xCo/C is used as CCL in the current generation of the Toyota Mirai fuel cell vehicles.^[60] Other particularly active candidates involve e.g. Cu, Ni or Pr as non-noble metal components.^[61,62,63] As mentioned earlier, increased temperatures can benefit the cell performance, e.g. due to accelerated reaction kinetics, improved water management or reduced CO poisoning of the ACL.^[64,65] However, as shown in the former section, the stability and degradation behavior of Pt/C in PEMFCs is also strongly linked to the cell operation temperature, which should similarly affect Pt alloy catalysts. Surprisingly, several supported Pt alloy electrocatalysts have already demonstrated superior stability over pure Pt/C at high temperatures.^[45,49,50,66,67,68]

In contrast to pure Pt/C, dissolution of the non-noble alloying element plays a central role in the durability of CCLs based on Pt_xM/C catalysts. In addition to affecting the ORR activity of the catalyst, dissolution of such elements can also lead to severe membrane poisoning, which further impedes an optimal PEMFC performance.^[69] Recently, Papadias *et al.* investigated the stability of different state-of-the-art commercial Pt_xCo/C catalysts with varying initial Co content (Catalyst H~34%, M~20%, L~15%), size (H~7 nm, M/L~4.5 nm) and morphology (H=porous, M/L=solid). In the study, these catalysts were subjected to ASTs under realistic simulated PEMFC operation conditions (80°C, 30000 cycles between 0.6

and 0.95 V).^[70] Even though catalyst H showed the highest mass activity at beginning of the test (BOT), which might be owed to the higher Co content or porous morphology, at end of test (EOT) most significant mass activity losses were observed for the same catalyst. As particle growth during AST was less pronounced in the case of catalyst H (due to the higher initial size), this observation cannot be mainly attributed to a loss of ECSA. Comparison of the specific activity (SA) to the Co content at BOT and EOT reveals that the decrease of SA almost linearly correlates with the decreasing Co content (Figure 5a). However, even though the relative decrease of Co of catalyst H and M during AST is almost similar (~50%), higher initial Co content seems to promote a faster degradation of the catalyst. Moreover, an impact of the porous catalyst structure on accelerated Co leaching should be considered. Consequently, the question arises, if temperature has a predominant role on accelerated ion leaching.

Indeed, results of Yano *et al.* indicate that over time, the Co content of Pt₃Co, immersed in 0.1 M HClO₄, decreases more strongly if the temperature is increased from 65 to 80°C, even without carrying out electrochemical measurements (Figure 5b).^[71] Besides, they found that the Co depletion rate also depends on the structure of the catalyst, as utilization of Pt₃Co with disordered crystal structure leads to reduced Co leaching compared to its ordered counterpart. Moreover, they observed that the fastest Co corrosion rate occurs during the first hours of immersion, which has previously been observed in real PEMFC applications.^[72] In addition, Pt₃Co/C generally has less tendency to produce H₂O₂ than pure Pt/C, which slows down the degradation of the catalyst. However, in case of alloy nanoparticles, the H₂O₂ production seems to be both, temperature-dependent and structure sensitive, while being almost constant in the case of pure Pt/C.

A particularly pronounced temperature-dependent decrease of the non-noble metal content was observed in the case of hollow PtNi nanoparticles. During AST experiments consisting of 5000 voltage cycles between 0.6 and 1.05 V vs RHE, the investigated electrocatalyst lost almost 100% of its initial Ni content at temperatures higher than 57°C, while at 25°C, the Ni content remained constant.^[73] As depicted in Figure 5c, the average crystallite size determined by X-ray diffraction (d_{XRD}) and average shell size determined by TEM (d_{TEM}) are influenced by the temperature of the AST. While at 25°C, the shell size remains approximately constant, temperatures above 80°C lead to a collapse of shell and central void and, in turn, formation of a spherical nanoparticle. As expected, in liquid electrolyte the accelerated degradation at higher temperatures triggers an enhanced loss of activity compared to degradation at room temperature.

A facile way to reduce the amount of (sub-)surface non-noble metal species, which are particularly prone to dissolution, and, in turn, enhance ORR activity and stability is so-called “dealloying” of Pt_xM/C-type electrocatalysts prior to operation. This involves the (electro-)chemical dissolution of the surface non-noble metal content, which previously showed promising results in rotating disk electrode (RDE) studies.^[74,75] In the first place, detailed investigations of dealloyed PtNi₃ during 10000

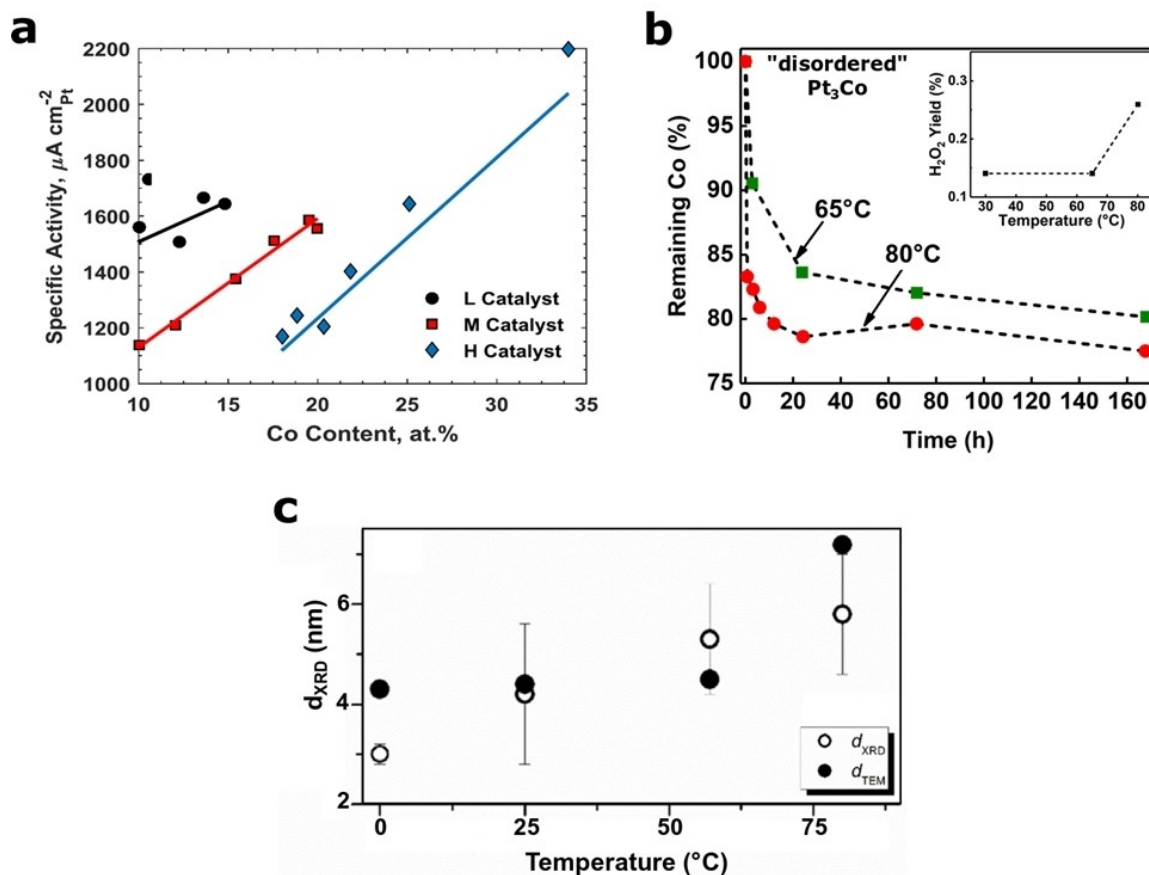


Figure 5. a) Specific activity as a function of Co content of different commercial Pt_xCo/C catalysts with high (H), medium (M) and low (L) Co content, compared at different stages of the AST. The data indicate that higher initial Co content results in higher initial activity, but also in accelerated degradation. Reused from Ref. [70] under the terms of a CC BY-NC-ND license. Copyright 2018 The Authors. b) Time-dependent decrease of the Co content of “disordered” Pt₃Co, immersed in 0.1 M HClO₄ at 65 °C and 80 °C, indicating accelerated and more pronounced Co leaching with increased temperature. The inset shows the H₂O₂ yield of the same catalyst as a function of temperature. The data values were obtained and replotted from Ref.^[71] c) Increase of the mean crystallite size (d_{XRD}) and shell size (d_{TEM}) of hollow PtNi/C with temperature, determined after ASTs. Adapted with permission from Ref. [73] Copyright 2019 Elsevier.

AST cycles (0.6–1.0 V vs RHE) at room temperature indicate that the decrease in Ni content is strongly size-dependent. While above 10 nm initial particle size a pronounced discrepancy is noted before and after ageing, especially between ~6 and 8 nm, the decrease in Ni content is comparably insignificant (Figure 6a).^[76] Superior ORR performance and durability of such structures was verified in a single-cell PEMFC setup, using dealloyed PtNi₃/C as active CCL material.^[77] In this study, the impact of the particle size (P1: ~8 nm initial diameter; P2: ~5 nm initial diameter) and the pretreatment protocol on the electrocatalytic performance of dealloyed PtNi₃/C was investigated under realistic operation conditions. In detail, pretreatment included the leaching in nitric acid (NA) and in sulfuric acid (SA), as well as thermal annealing (AN). The investigations indicate that both, the initial particle size as well as the Ni content influence the activity and durability of the catalyst. Overall, the smaller particles (P2) show a better mass activity after MEA conditioning. It is noticeable that, despite the same pretreatment with nitric acid, the smaller particles retain higher Ni content. The authors justified this with the susceptibility of larger particles to form nanoporous structures, while the smaller

particles are able to form a stable Pt-rich shell, which “passivates” the particles in further durability tests. Moreover, less oxidative acid treatment and annealing seem to further benefit Ni retention. Accordingly, after 30000 AST cycles, the smaller particles show significantly better activity retention, probably due to the higher Ni content. However, the results confirm that, despite dealloying, in a certain range of size the Ni content drops sharply during AST at high temperatures, while being rather stable at room temperature (Figure 6a, b).

As mentioned earlier, particle morphology and shape stability are other crucial parameters that influence catalyst durability at elevated temperatures. In particular, this accounts for particles with non-trivial shapes (e.g. nanoframes, hollow particles, rods),^[78,79,80] which have been found to show improved ORR kinetics compared to their purely spherical analogues. TEM studies on the degradation of structurally disordered sponge PtNi/C and structurally ordered octahedron PtNi/C amongst voltage cycling in RDE at 80 °C indicate that in the case of sponge PtNi/C, the disordered structure remains fairly intact over the course of 20000 AST cycles (0.6–1.0 V vs RHE).^[81] In contrast, one observes that temperature has a devastating

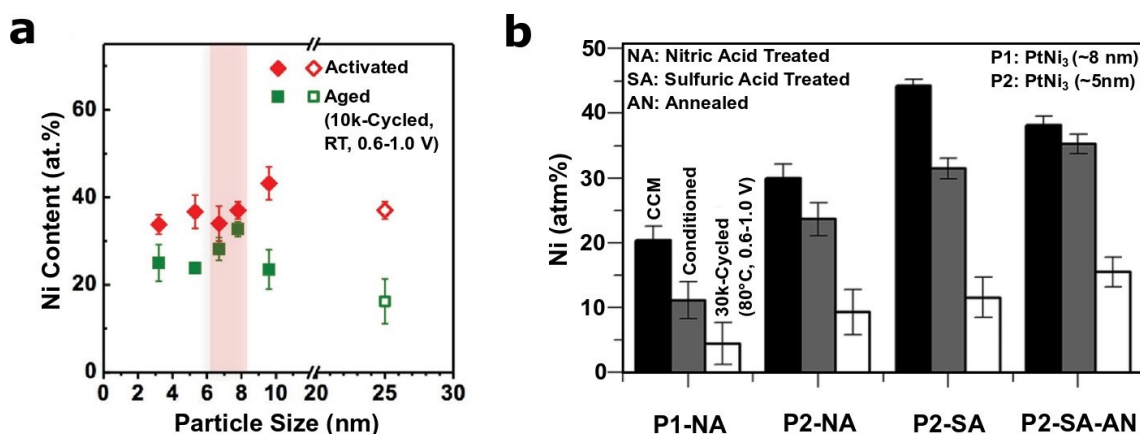


Figure 6. a) Ni content of PtNi₃ as a function of the nanoparticle size, compared before and after 10000 voltage cycles in RDE at room temperature. Best Ni retention was observed at a particle size ranging between ~6 and 8 nm. Adapted with permission from Ref.^[76] Copyright 2016 Wiley-VCH. b) Change of the Ni content of differently treated PtNi₃-based catalyst coated membranes (CCMs) within voltage cycling in a single-cell PEMFC at 80 °C. Overall, lower initial particle size, less oxidative acid pretreatment and thermal annealing were found to effectively suppress Ni leaching. However, compared to cycling at room temperature, Ni leaching is strongly pronounced. P1 = commercial PtNi₃/C with ~8 nm initial average diameter; P2 = commercial PtNi₃/C with ~5 nm initial average diameter; NA = Nitric acid treatment; SA = Sulfuric acid treatment; AN = Thermally annealed. Adapted from Ref. [77] under the terms of a CC-BY 3.0 license. Copyright 2015 The Authors.

effect on the shape of octahedral PtNi/C, which loses its order within less than 5000 AST cycles. These observations are closely reflected by the change of activity during voltage cycling. While initially octahedron PtNi/C outperforms sponge PtNi/C, especially in terms of specific activity, it is visible that the disordered shape has a beneficial effect on stability, leading to an improved mass activity compared the octahedron-shaped catalyst after the AST. In the case of hollow PtNi/C particles

introduced earlier, Dubau *et al.* monitored the influence of temperature on the particle structure using high-angle annular dark-field scanning transmission electron microscopy (HAADF-STEM) and energy dispersive X-ray spectroscopy (EDX).^[73] While the particle structure remained largely constant at over 5000 cycles at 25 °C, the shell thickness increased with increasing temperature and no ring structure could not be preserved after ASTs at 80 °C (Figure 7).

Degradation of Hollow PtNi/C at various temperatures

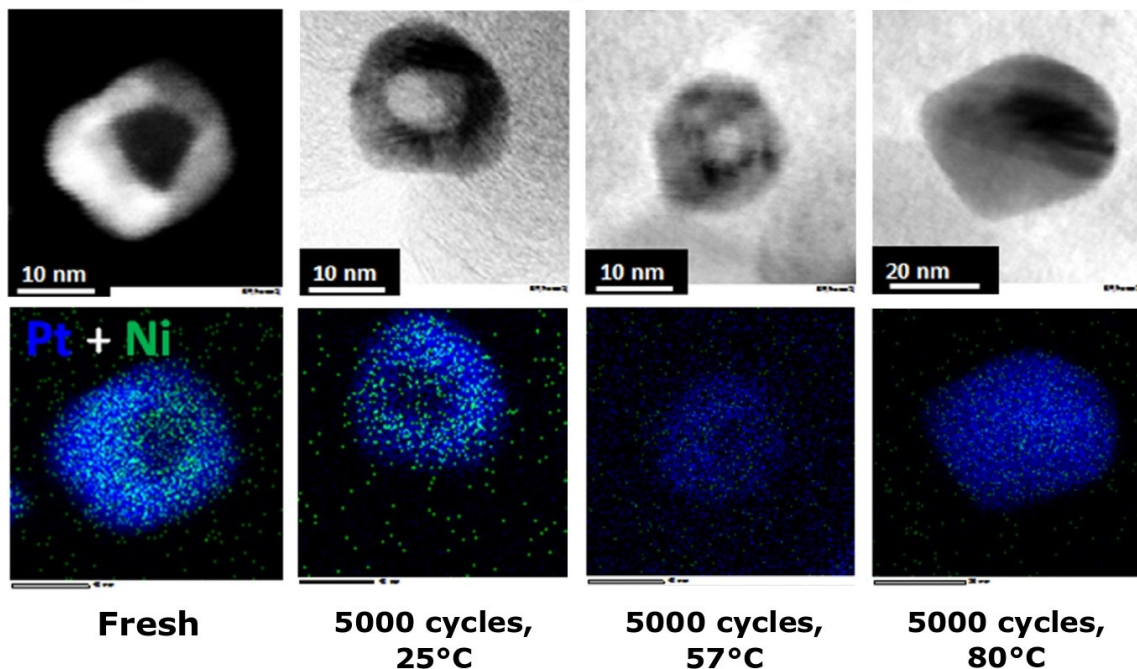


Figure 7. Degradation of hollow PtNi/C within voltage cycling (5000 cycles, 0.6–1.05 V vs RHE) at different temperatures, monitored via HAADF-STEM and EDX. While the structure of hollow PtNi/C survives the AST at room temperature, 80 °C lead to the formation of solid PtNi/C. Adapted with permission from Ref. [73] Copyright 2015 Elsevier.

Again, these observations confirm that temperature has a determining effect on PEMFC catalyst durability, i.e. alloy composition and particle shape are highly sensible to PEMFC operation temperatures.

3.2. Effect of Temperature on the Degradation of the Gas Diffusion Layer

In PEM fuel cells, the GDL enables transport of reactant gases from flow channels to the CL, accompanied by draining the produced water at the CLs.^[82,83,84,85,86] In addition, the GDL also needs to be a good electron conductor regarding current collection. There are various types of GDLs in development, however, in general they are made of porous carbon fiber and carbon particles.^[87] A schematic depiction of the GDL is shown in Figure 8a, where the macroporous substrate and MPL are displayed.^[88] The main function of the substrate is to distribute

the reactant gases and to collect the current. The MPL consists of carbon powder and hydrophobic groups (polytetrafluoroethylene polymers) that manage the water flow. Therefore, mechanical strength, conductivity and hydrophobicity are core characteristics of the GDL.

There are several GDL degradation mechanisms such as chemical degradation, erosion by gas flow, dissolution by water, freeze/ thaw effect and mechanical compression effects. Up to now, there are only handful of articles, which explore the influence of temperature on GDLs. Within this section, we summarized some of the studies on GDL degradation caused by temperature changes. More detailed overall reviews specifically focusing on GDLs can be found elsewhere.^[83,89]

The durability of the PEM fuel cell largely depends on the stability of the GDL. In fact, there are several GDL degradation mechanisms such as chemical degradation, erosion by gas flow, dissolution by water, freeze/ thaw effect and mechanical compression effects. Herein, we will highlight GDL degradation

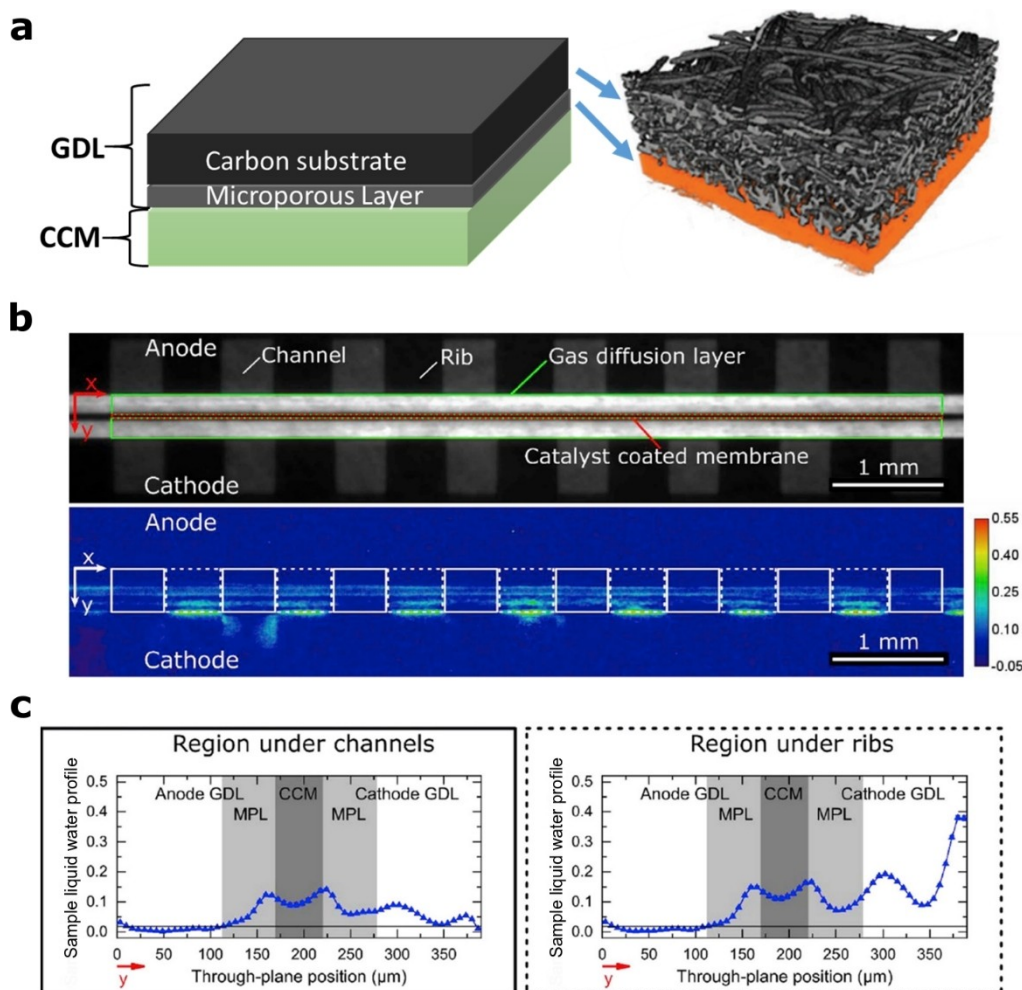


Figure 8. a) Schematic depiction of the GDL structure. The volume rendered image on the left is adapted with permission from Ref. [88] Copyright 2017 American Chemical Society. b) Radiograph showing the assembled fuel cell components. The arrows in the figure show the directions of x- and y- axes (the direction of the z-axis goes into the plane of the figure). The boundaries of each component are also shown in the image for clarity. Processed image depicts the liquid water distribution inside the cell. The thickness of the liquid water is indicated in the legend. The dotted lines show the regions under the ribs and solid lines indicate the regions under the channels. c) The graph showing normalized liquid water amount along the y-axis of the cell. Figures (b) and (c) are taken with permission from Ref. [92] Copyright 2018 Elsevier.

caused by temperature changes. For instance, during winter times, PEMFCs are exposed to temperatures below the freezing point of water, especially in automotive applications. At these low temperatures, the water residues inside the cell can freeze, resulting in conductivity losses.^[90] Lim et al^[90] investigated the changes in the cell resistivity over number of freeze/thaw cycles between -30°C to 70°C using different types of GDLs, namely carbon cloth, paper-type and felt-type carbon. The felt-type GDL showed the least increase in the ohmic resistance of the cell (R_{ohm}), whereas both carbon-cloth and paper-type GDLs resulted in rapid increase in the R_{ohm} . Interestingly, the charge transfer resistance (R_c) of the cells with all three types of GDLs did not increase with thermal cycling, indicating that freezing temperatures did not significantly influence the charge transfer resistance of the cell. Apart from increasing the cell resistance, any droplets of water will cause certain volume expansion and generate mechanical stress on porous PEMFC components such as GDL.^[91] More detailed discussion about the mechanical degradation of GDLs due to ice formation is discussed above in section 2.2. Therefore, there are various methods for in-operando liquid water visualization inside a fuel cell, such as synchrotron X-ray radiographic imaging.^[92,93] Figure 8b shows both, the radiograph and processed image of an assembled single cell. The amount of liquid water along the cells is given in Figure 8c, where the water distribution inside different cell components under the ribs and channels is distinguished. This methodology enables the identification of the regions where liquid water accumulates and highlights the regions where damages can occur when starting the cell at sub-freezing temperatures.

3.3. Effect of Temperature on the Degradation of the Proton Exchange Membrane

In PEMFCs, the task of the membrane, sandwiched between the two CLs, is to transport protons, support the catalyst layers and separate the reactions occurring at the anode and the cathode side. Therefore, a suitable membrane material should meet the requirements of a high proton and low electron conductivity, low fuel and oxidant permeability, high mechanical and chemical stability, and low cost. Besides, the aforementioned properties should be maintained at both, low and elevated temperatures. Low temperatures may occur during operation of e.g. a FCEV during cold ambient temperatures. The following considerations, however, will focus on operation of a PEM membrane at elevated temperatures. The subject of freezing temperatures on performance and durability is addressed in Section 2 and further discussed elsewhere.^[96,97] Elevated operational temperatures help to circumvent CO poisoning, increase diffusion rates and promote operational conditions, such as reduced cooling and lower pressurization at lower humidity.^[7] Unfortunately, certain degradation mechanism are accelerated with increasing temperature, and have to be overcome by sophisticated material design.

In the following, a short overview on different types of proton conduction, degradation mechanisms and their mitiga-

tion will be discussed. Hereby, the focus will be on the most widely used type of material in PEMFCs, namely poly(perfluorosulfonic) acid (PFSA) polymers. Commercially available membrane materials include Nafion[®] (DuPont), AQUIVION (Solvay Solexis), Aciplex and Flemion (Asahi Kasei). Additionally, an alternative class of materials will be discussed, namely sulfonated hydrocarbon membranes.

Among all PFSA polymers, Nafion[®] is the most prominent one, due to its high proton conductivity of up to 0.1 S cm^{-1} . This outstanding property can be ascribed to its structure, consisting of a tetrafluoroethylene (PTFE) backbone and sulfonic acid groups present at the end of the side chains. The former is responsible for the membrane stability and the latter provides sites for proton transport. At a certain level of hydration, Nafion[®] is able to self-align into a backbone-rich hydrophobic phase and a side chain-rich hydrophilic phase. Thereby, water-filled channels and voids are created, consisting of walls built up by sulfonic acid groups. This sponge-like structure is shown in Figure 9a, accompanied by its structure formula. Mechanistically, a proton can detach from the sulfonic acid groups, be transferred to a nearby water molecule and thus form hydronium. Alongside with this hydronium, protons can be transported through a percolated network by two different types of conduction: the (1) Grotthus and (2) the vehicle mechanism. At low hydration rates, the latter is present.^[7] This means that protons can diffuse through the membrane using hydronium as a carrier or in the form of hydrated proton complexes.^[7,98] At higher level of hydration, a percolating network of hydrogen bonds may eventually be formed. Following the Grotthus mechanism, the proton can hop along this chain of hydrogen bonds by subsequent breaking and reforming hydrogen bonds. Both mechanisms are schematized in Figure 9b.

Even though PFSA membranes exhibit high thermal and chemical stability, they face serious degradation problems at elevated temperatures. At temperatures above 100°C , dehydration is likely to occur due to evaporation of the water within the pores of the membrane. This leads to interruptions in the hydrogen bond network, and eventually in a decrease of conductivity. This can also be observed in thermal gravimetric analysis (TGA)^[95] of Nafion[®] 117, as depicted in Figure 9c, part I. With increasing temperature, the membrane will lose its conductivity via a partial decomposition of sulfonate groups, oxidation of the ends of the side chain and finally decomposition of the perfluorinated matrix (Figure 9c, parts II–IV).^[96] Apart from the loss in proton conductivity, dehydration at higher temperatures is also negatively interrelated to the mechanical stability of the membrane. Being exposed to dry conditions for longer times can lead to brittleness and the occurrence of cracks. This enables gas crossover and uncontrolled reaction between hydrogen and oxygen, which results in a cycle of hot spot and pinhole formation, and ultimately to the destruction of the membrane. Note that the term 'hot spot' usually indicates a region of high reaction and current densities and does not necessarily refer to temperature. Gas crossover facilitates the production of hydrogen peroxide (H_2O_2) at the anode but can also be formed as a side product at the cathode. Formation of H_2O_2 can lead to the presence of hydroxyl (OH)

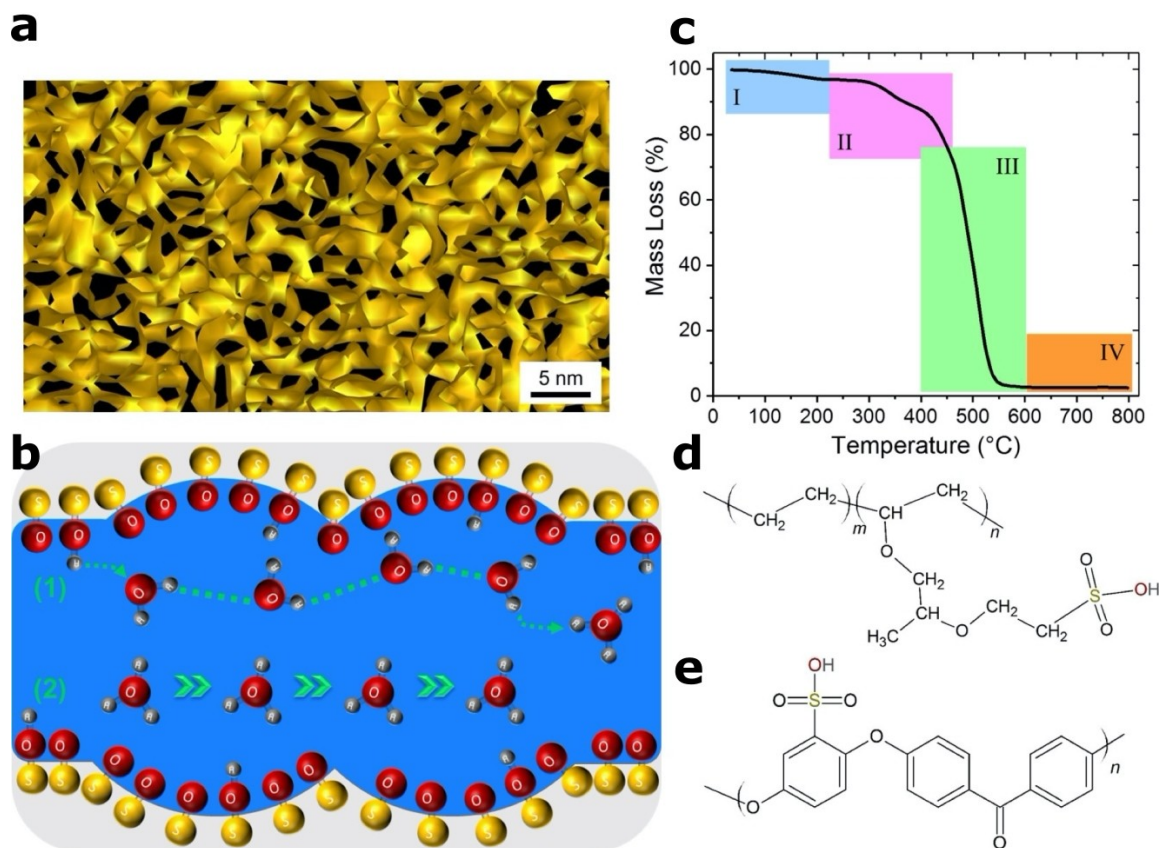


Figure 9. a) Structure of the most commonly used proton-conducting PFSA membrane material; Nafion®. The structure of the hydrated Nafion® film was obtained by TEM reconstruction and is reproduced with permission from Ref.^[94] Copyright 2015 American Chemical Society. Here, an interconnected network of hydrophilic domains can be seen (colored in yellow). b) The separation of hydrophobic and hydrophilic parts of PFSA-type polymers leads to the formation of reversed micelles. Within these water-filled channels, protons can be conducted either by 1) the Grotthus or 2) the vehicle mechanism. Sulfur, oxygen and hydrogen atoms are colored in yellow, red and gray, respectively. c) Thermal decomposition of Nafion®. The curve obtained by thermogravimetric analysis is adapted with permission from Ref.^[95] Copyright 2015 Springer Nature. The curve is divided into different degradation mechanisms occurring with increasing temperature: I) dry out of the formerly hydrated membrane, II) decomposition of the sulfonate groups, III) further oxidation of the side-chain and breaking of carbon-sulfur bonds and IV) the decomposition of the complete backbone.^[96] Structure formulas of d) Nafion® and one of its alternatives e) the sulfonated hydrocarbon SPEEK.

and peroxy (OOH) radicals which attack the polymer end groups of the membrane. These unwanted reactions are accelerated at low humidification and elevated temperatures.^[99,100] Besides, trace metal ions stemming from either the corrosion of metal bipolar or end plates, as well as from the leaching of the less noble metal of an alloy catalyst can settle down in the membrane.^[69] These are able to act as catalysts for the aforementioned radical attacks and can, therein, accelerate membrane thinning and failure. Therefore, an interplay of dehydration, mechanical and chemical degradation, which is accelerated at elevated temperatures, has to be overcome in order to optimize operation of PEMFCs at higher temperatures.

In order to receive the benefits coming with a PEMFC operated at higher temperatures, different mitigation approaches have been reported in literature to avoid the above-mentioned degradation processes. Concerning the group of PFSA membranes, these strategies can roughly be divided into a modification of the actual polymer structure or into the formation of hybrid membrane. These hybrids usually consist of

the combination of the polymer material with inorganic or organic fillers. Besides, different non-PFSA membrane have been developed that will shortly be mentioned in the end of this report.

A well-known means to alter the structure of PFSA polymers is to tune their side chain length. This will influence their morphology and thus the structure of the percolation pathway of the proton transport. Using short-side chain (SSC) PFSA comes with the advantage of a higher crystallinity and better connected aqueous domains.^[101] A higher density of sulfonate ions can improve phase separation.^[102] Besides, modifying side chains comes with the ability to eliminate groups that are prone to degradation.^[101] Nonetheless, due to their similarity to “normal” PFSA, SSC PFSA still suffer from low conductivity at low water contents and low mechanical strength at high temperatures.^[98]

Therefore, additional hybrid approaches are applied to overcome implied shortcomings. In this regard, nanoparticles incorporated in the polymer matrix can interact with the ionomer. Due to their high specific surface area, these surface

interactions can tune the original properties of the polymer membrane. The behavior of the herein established hybrid membrane depends naturally on the type, size and shape of the nanoparticles. In principle, the used materials can be subdivided into two groups, hygroscopic materials and materials that contribute to the proton conductivity. The former ones can roughly be assigned to metal oxides and the latter is mostly carbon-based.

A well-known class of fillers are metal oxides (MO_2), such as silica, zirconium or titanium oxide. Due to their hygroscopic nature, water molecules can adsorb onto them and thus increase the water uptake at higher temperatures and lower humidification.^[103,104] At a certain concentration, cross-linking of the polymer is possible via M–O–M bridges, which can additionally stabilize the membrane.^[105] However, a too high concentration of metal oxide fillers can pose a barrier to water molecules or mask the SO_3H groups at the end of the polymer side chains.^[106] This leads to a sudden decrease in proton conductivity. In order to increase the pristine proton conductivity of the oxides, a common step is to functionalize their surface with proton-conducting groups, e.g. sulfonated metal oxides.^[107,108] Another possible application of metal oxides in polymer hybrids is their utilization as ‘scavenger radicals’. In detail, transition-metal oxides, such as e.g. manganese- or cerium-based, react with occurring oxo-radicals before they react with the ionomer chain or crossover gases, and therefore chemically stabilize the membrane.^[109] Overall, such hybrid composites possess an increased performance at higher temperatures and lower humidity.^[110,111] However, a stable long-time performance of these hybrid materials is yet to be demonstrated.

A desirable shape of additives would be one wide-spread dimension to ensure good proton transport in one direction and two narrow dimensions to disperse the additive in the polymer matrix. Carbon nanotubes (CNT) possess these dimensions and their high elastic modulus assures good proton conductivity. However, they come with an inherent drawback regarding their electronic conductivity. In order to avoid a short circuit of the PEMFC, the amount of CNT should be well below the percolation threshold. Adding CNTs to the polymer membrane can increase its mechanical stability^[112] and assist in building water channels.^[113] However, in order to directly contribute to proton transport, they have to be equipped with proton adsorption site containing materials, such as imidazole groups.^[114]

A possibly cheaper alternative to PFSA polymers with high thermal and mechanical stabilities are sulfonated hydrocarbon membranes.^[7,115] As an example, the structure formula of sulfonated hydrocarbon Sulfonated Poly(Ether Ether Ketone) (SPEEK) is given in Figure 9d. However, the phase separation of hydrophilic and hydrophobic moieties is low and thus also their intrinsic proton conductivity. This drawback can be overcome during synthesis of copolymers, tuning the architecture of the membranes.^[116] Moreover, base-doping with pyrazole, triazole, and tetrazoles is a way of introducing additional proton acceptors and thus increasing the conductivity.^[98]

4. Cross Influences between Temperature and other Operational Parameters

The performance of PEM fuel cells is affected by several parameters; these include temperature, pressure, and relative humidity (RH). This review focuses mainly on the effect of temperature on low-temperature PEM fuel cell performance, but other parameters that the temperature can influence, such as relative humidity (RH) and the partial pressure of operating gasses, will be briefly discussed.

4.1. Effect of Relative Humidity (RH) on PEM Fuel Cell Performance

The RH at a specific temperature, $RH(T)$, is defined as the amount of water vapor in the air, i.e., the partial pressure of water ($P_{\text{H}_2\text{O}}$) relative to the maximum amount that air can hold, i.e., the saturated vapor pressure above water ($P_{\text{H}_2\text{O}}^0$), and is expressed as a percentage value.

$$RH(T) = \frac{P_{\text{H}_2\text{O}}(T)}{P_{\text{H}_2\text{O}}^0(T)} \times 100$$

During PEMFC operation, protons formed at the anode side will move through the PEM to the cathode, where they transfer in the membrane in the form of hydrated protons carried by water. The larger the number of protons moving through the membrane, the greater the amount of water that moves from anode to cathode. Because of water penetration through the membrane, the water content decreases at the anode side and increases at the cathode side. This concentration difference leads to a water back diffusion to the anode.

Membrane dehydration results in poor proton transfer, reduced ionic conductivity, and increased ohmic resistance. For maintaining the membrane sufficiently hydrated, the hydrogen must be humidified. When air is used at the cathode instead of pure oxygen, the air flow rate is increased to maintain a high oxygen concentration at the cathode, which makes the water loss at the anode side more severe. Therefore, the air must also be humidified. Means of water transmission in the PEM are described in Figure 10.^[117]

If the water content in the membrane is too high, liquid water can form from saturated water vapor, diluting the concentration of the reactive gas and blocking the pores of the GDL, which in turn results in oxygen mass transport limitation. Therefore, maintaining appropriate water content is crucial for the fuel cell performance and several experimental and modeling studies focused on this issue.^[118,119,120,121,122]

When membrane electrode dehydration occurs, membrane conductivity decreases and ohmic resistance increases, resulting in a significant fuel cell voltage loss, which leads the fuel cell polarization curve to decrease with decreasing RH.

Low RH makes thermal management of the fuel cell difficult. As the resistance of membrane increases, the output voltage drops, and to achieve the same power, the output current must

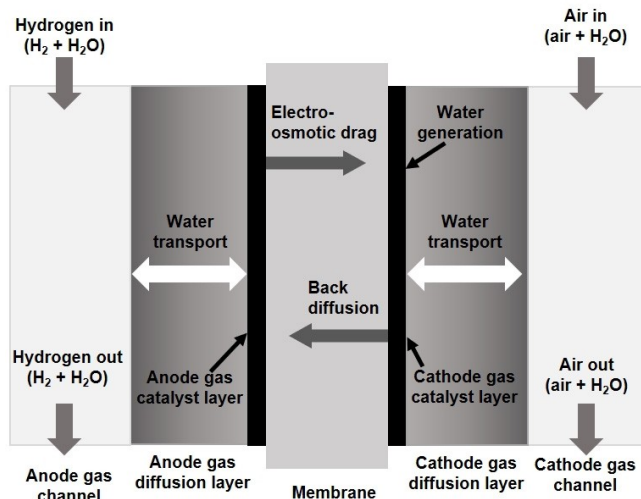


Figure 10. Schematic of means of water transmission in a typical hydrogen PEMFC. Adapted with permission from Ref. [117] Copyright 2006 Elsevier.

increase. This results in increasing the fuel cell temperature, in turn decreasing the RH even further, and leading to a continuous deterioration in fuel cell performance.

4.2. Effect of Cathode Humidity on Overall Cell Performance

To reduce the air-drying effects on the membrane, the cathode needs to be humidified. At a constant anode RH, the membrane's water content increases due to water diffusion

from cathode to anode. Under a high current density, the amount of water moving along with protons from anode to cathode will be greater than the water back-diffusion from cathode to anode. Therefore, at low anode RH, the fuel cell performance improves with increasing the cathode RH. A high anode RH, this humidification can to some extent compensate for the loss of membrane water content, therefore high cathode RH can decrease the oxygen partial pressure in air, and even a flooding of the cathode, resulting in decreased fuel cell performance (see Figure 11).^[117]

On the other hand, as water is continuously forming at the cathode side, the RH is generally high. If the cathode RH is low, the membrane water content will not be uniform, resulting in lower RH at the GDL/catalyst layer interface and higher RH in membrane/catalyst layer interface, and resulting in uneven current density distributions.

4.3. Effect of Anode Humidity on Overall Cell Performance

If the cathode RH is very low, <20%, increasing the anode RH enhances the membrane performance, while if the cathode RH is high, the water back-diffusion can maintain the membrane humidified when the anode RH is low. On the other hand, if the anode RH increases, the hydrogen partial pressure decreases and in this case the anode RH has little effect on cell performance (see Figure 12).

In general, the fuel cell performance can be enhanced by keeping cathode RH close to 100%, while reducing anode RH. A 100% RH at the cathode side ensures the membrane humidification. A relatively low RH at the anode side enables water

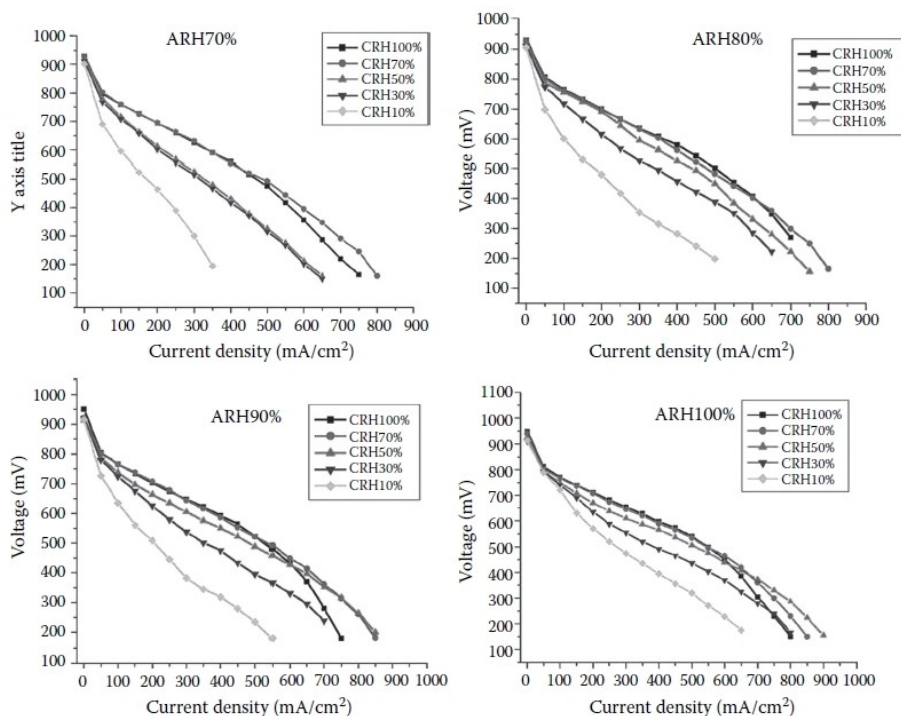


Figure 11. Polarization curves for a fuel cell operated at different air relative humidity. Reprinted with permission from Ref. [117] Copyright 2006 Elsevier.

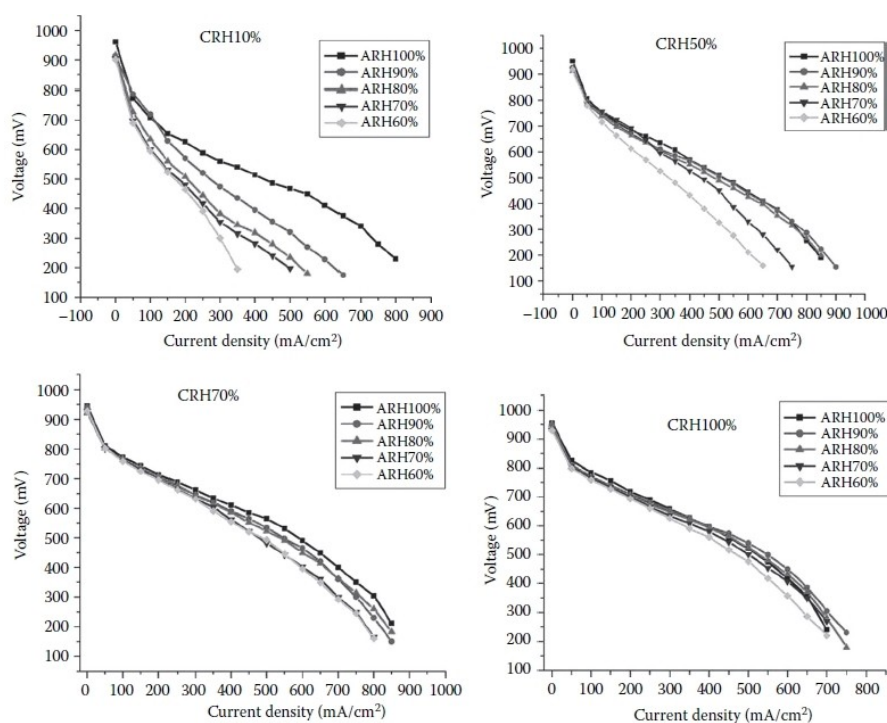


Figure 12. Polarization curves for a fuel cell operated at different anode relative humidity values. Reprinted with permission from Ref. [117] Copyright 2006 Elsevier.

back-diffusion from cathode to anode, especially at low operating voltage, where the cathode produces large amounts of liquid water. This back-diffusion keeps the membrane humidified and alleviates water flooding at the cathode side, thus reducing mass transfer loss and ultimately increasing fuel cell performance.^[120]

4.4. Effect of Relative Humidity on ORR Kinetics in a PEMFC

The effect of relative humidity on the ORR kinetics was investigated in only a few studies, where poor ORR kinetics were correlated to low RH values.^[123,124,125] Uribe *et al.* was one of the first groups to investigate the effect of RH on ORR kinetics and they proposed that poor ORR kinetics at low RHs results from the surface restructuring of the ionomer in which hydrophobic components would come into contact with the Pt surface.^[126] Xu *et al.* found that there is 85 mV increase in overpotential as RH was changed from 100% to 40%, and they suggested that this poor ORR kinetics is due to a lowering in the proton activity coefficient, the use of an alternate reaction mechanism, or a combination of both.^[124]

Neyerlin *et al.* examined the effect of RH on ORR kinetics, where a differential cell was used to achieve a steady state and provide mass-transport-free operating conditions. In that study, the current density at 0.3 V overpotential was chosen to evaluate the ORR at constant temperature and various relative humidity values.^[123] The study concluded that the RH has a strong effect on the ORR catalytic activity under dry conditions (0–60%), while at higher RHs, no significant effect was found

(see Figure 13). The Tafel slope was found to be around 80 mV/dec for wet conditions, while it is about 100 mV/dec for dry conditions. The ORR activation energy was found to be 49 kJ/mol at 100% RH, while a 55 kJ/mol activation energy was measured at 50% RH. The authors concluded that the dependence of the ORR kinetics on the RH may be explained by the changes of the rate-determining step, proton activity, and adsorbed -OH on the platinum surface.

4.5. Effect of RH on PEM Fuel Cell Start-Up/Shut-Down Losses

For automotive applications of PEMFCs, increasing the lifetime of MEAs is one of the main challenges, especially during start-up/shut-down (SUSD) cycles. During SUSD, the cathode carbon support oxidizes as a result of hydrogen/air_{anode} gas fronts moving through the anode. An SUSD event takes place when a hydrogen/air_{anode} gas front moves through the fuel cell anode.^[127] This event invokes oxidative currents on the cathode side, as a result of the corrosion of the cathode carbon support.

Temperature and RH are considered the major parameters affecting the carbon oxidation reaction (COR) in a fuel cell. Lim *et al.* investigated the effect of RH on the carbon corrosion rate by carrying out corrosion experiments at 1.4 V vs RHE (reversible hydrogen electrode potential) at various temperatures, while keeping the water vapor partial pressure constant.^[128]

Kreitmeier *et al.* and Ofstad *et al.* studied the effect of RH at 80 °C on the SUSD degradation using on-line CO₂ measurements, showing a positive correlation of the COR and the RH

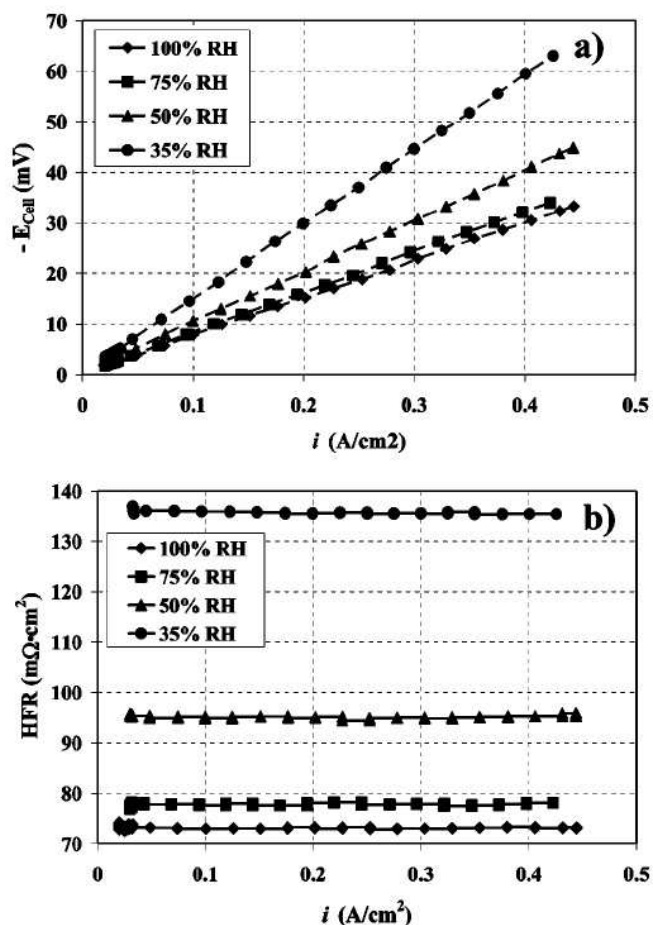


Figure 13. a) Cell voltage vs current density for a hydrogen concentration cell operating at 300 kPa_{abs} and 55 °C with a flow rate of 1000 sccm of H₂ for four different RH values. b) HFR vs current density. Same conditions as in (a). Reprinted with permission from Ref. [117] Copyright 2006 Elsevier.

deduced from.^[129,130] Recently, the PEMFC performance loss was observed over extended SUSD cycles and it was combined with a prediction of the carbon oxidation reaction rate at various temperatures.^[51]

Mittermeier *et al.* reported a study on the prediction and experimental determination of the SUSD damage induced by extended H₂/air_{anode} gas fronts as a function of RH.^[131] To achieve this goal, the authors utilized on-line mass spectrometry in order to quantitatively determine the COR rate at 80 °C vs potential and RH, and therefore determined the COR reaction order with respect to the RH. Figure 14 shows Polarization curves recorded before and after 60 SUSD cycles at 0.25, 0.4, 0.66, 0.80, 1.00 and wet RH, where “wet” denotes over-humidified gas at the inlet, with a minimum RH of 1.20.^[131]

For MEAs with electrodes based on Pt catalyst supported on high surface area carbon, the SUSD-induced degradation rate (expressed as mV cycle⁻¹ s⁻¹) was found to decrease by a factor of about 3 when the RH was reduced from 1.00 to 0.25 at 80 °C during SUSD events. Very recent studies confirmed this finding under similar operating conditions.^[132]

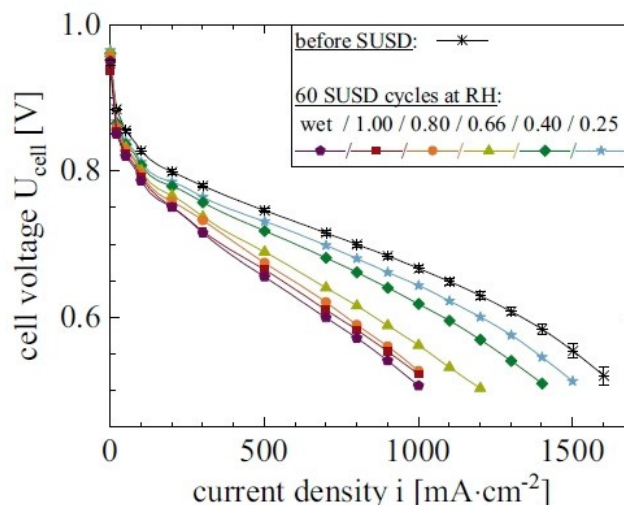


Figure 14. Polarization curves recorded before (asterisks) and after 60 SUSD cycles at various RHs (colors/lines defined in the figure). H₂/air polarization curve conditions: T_{cell} = 80 °C, RH = 0.66, p_{cell} = 170 kPa_{inlet,abs}, stoichiometry = 1.5H₂/1.8air. SUSD conditions: T_{cell} = 80 °C, various RH, P_{dry gases} = 101 kPa_{inlet,abs}. (Further experimental details can be found in the original study).^[131]

4.6. Effect of Partial Pressure of Operating Gasses on Overall Cell Performance

In general, the effect of the reactant gas partial pressure on the fuel cell performance is observed in a wide range of pressures, from ambient to 5 atm. The higher the reactant partial pressure, the higher the apparent exchange current density, leading to an enhanced performance. In this review, we focus only on the partial pressure changes that are caused by the operating temperature. The exchange current density is related to the reactant partial pressure through Equations (1) and (2):

$$i_{\text{O}_2}^0 = (\text{EPSA})_c i_{\text{O}_2(\text{Pt/PtO})}^0 \left(\frac{P_{\text{O}_2}}{P_{\text{O}_2}^0} \right)^{0.001678T} \quad (1)$$

$$i_{\text{H}_2}^0 = (\text{EPSA})_a i_{\text{H}_2(\text{Pt})}^0 \left(\frac{P_{\text{H}_2}}{P_{\text{H}_2}^0} \right)^{0.5} \quad (2)$$

where (EPSA)_a and (EPSA)_c are the electrochemical Pt surface areas of the anode and cathode catalyst layers, respectively. $i_{\text{H}_2(\text{Pt})}^0$ and $i_{\text{O}_2(\text{Pt/PtO})}^0$ are the intrinsic exchange current density of H₂ and O₂ on Pt and Pt/PtO surface, respectively. $P_{\text{H}_2}^0$ and $P_{\text{O}_2}^0$ are the standard pressure of H₂ and O₂, respectively.^[133]

Through a numerical study, Esfah *et al.* showed that the change in the partial pressure of hydrogen and oxygen is not significant due to fluctuation in the operating temperature of 60 °C to 80 °C, which a decrease of about 20% is expected when the temperature increases from 80 °C to 100 °C (Figure 15).^[134] These changes in reactant partial pressure are insignificant compared to the inlet and outlet pressures that can be controlled externally.

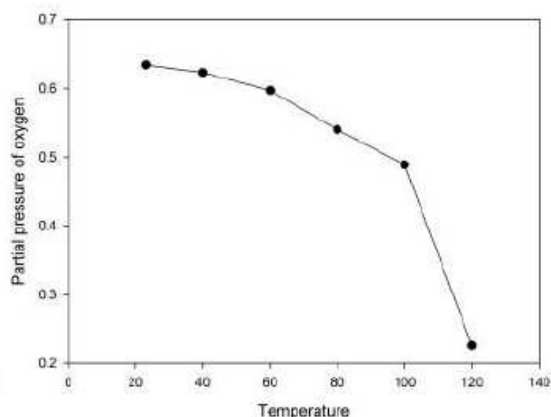


Figure 15. Effect of the operating temperature on partial pressure of a) hydrogen and b) oxygen. The figure is adapted with permission from Ref. [134] Copyright 2014 Elsevier.

5. Thermal Management of PEMFCs

Fuel cells generate an amount of waste heat similar to their electric power output. The heat generation arises from entropic

heat of reaction, irreversible electrochemical reactions, ohmic losses and water condensation. Next to performance losses, PEMFCs show only little tolerance to temperature distributions due to the aforementioned degradation of their components at high temperatures. Therefore, a proper thermal management is inevitable for an optimized and constant power output. Typical cooling systems can roughly be divided into three categories as sketched in Figure 16a: (1) liquid cooling, (2) indirect cooling and (3) air-cooling.^[137] The choice of cooling system largely depends on the power output of the stack: For stacks in the range of 200 W–2 kW air-cooling can be beneficial, whereas for stacks with significantly larger power output liquid cooling is required.^[138,139] Thermal management can be probed by accessing the temperature distribution across a stack either experimentally (see section 2) or by modelling. Details of the latter are summarized in a recent review article.^[140]

In many PEMFC stacks, a cooling circuit is integrated in the BPPs separating the anode and cathode of adjacent single cells. Thus, excess heat can be removed by forced convection. Different liquids can be employed as coolant such as ethanol, methanol and acetone,^[141] nanofluids,^[142] but also water.^[143] Using conventional water as cooling medium possesses the advantage of being combinable with the humidifier for the gas

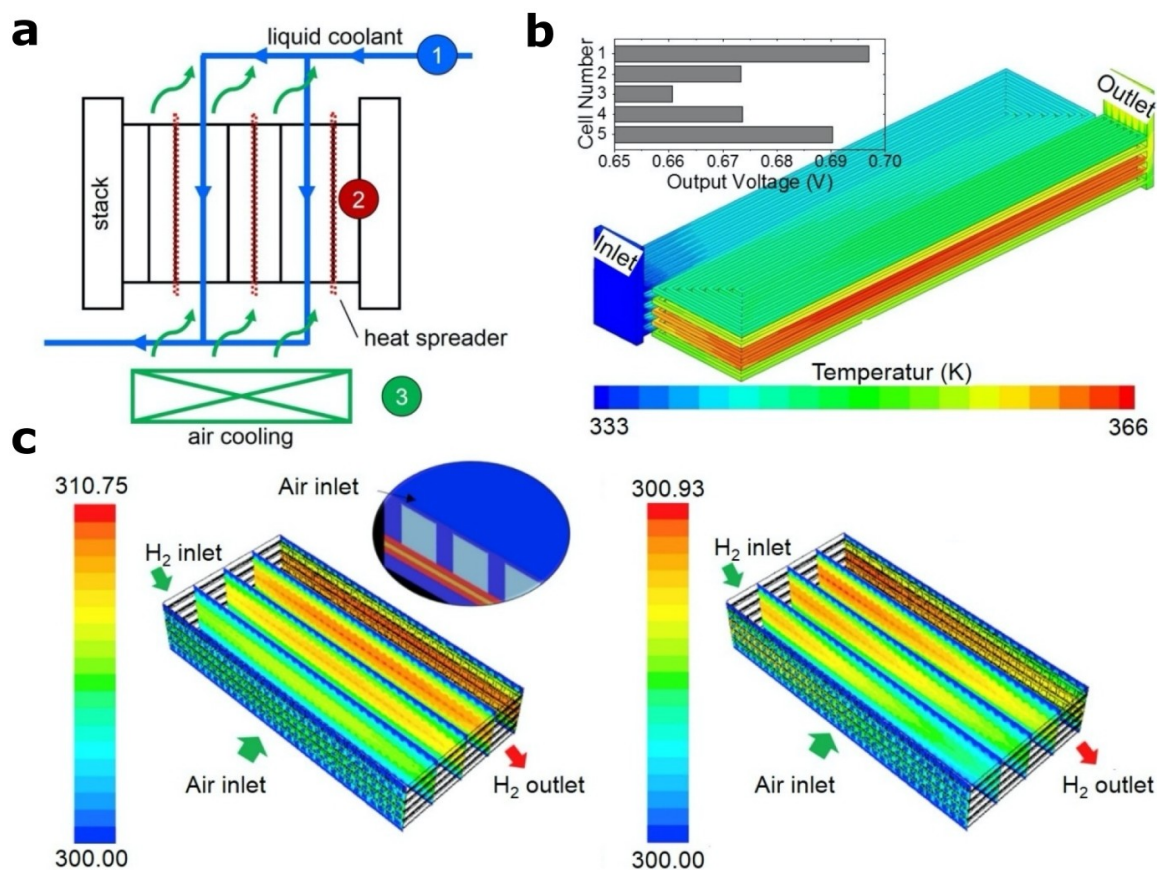


Figure 16. a) Thermal management can be provided via three cooling principles: 1) liquid cooling, 2) the insertion of a heat spreader and 3) air-cooling. Different temperature distributions across a PEMFC stack were obtained by modeling for b) liquid cooling and c) open-cathode air-cooling. The inset in (b) shows the voltage output of every single cell, while in (c) the temperature distribution was modelled for two different operational voltages (left: 0.6 V, right: 0.8 V). In both cases, a PEMFC consisting of five cells was investigated; however, different modelling approaches were applied. Figure (b) and (c) were created (adapted) by reprinting data and figures with permission from Refs. [135, 136] Copyright 2019 Elsevier and Copyright 2016 Elsevier, respectively.

supply. Besides adjusting the coolant, e.g., according to its cooling capacity, the design of the channels in the cooling flow plate can help to achieve a uniform temperature distribution across the stack. Cooling circuits with various designs have been tested and their thermal properties have been addressed either experimentally,^[144,145] or by modelling.^[136,146,147,148] An example how to access the temperature distribution of a liquid cooled fuel cell stack by three-dimensional (3D) multiphase non-isothermal modelling is given in Figure 16b. The authors probed the influence of temperature on oxygen and liquid water content, current density, membrane hydration and performance of a five cell-containing stack.^[135] The simulated stack was cooled by a single cooling unit sandwiching the stack from above and below, using water as coolant. Figure 16b shows the temperature distribution in the anode/cathode flow fields, being designed as 7-path serpentine flow with two U-turns. It can be seen that the difference in temperatures of the stack is as high as 30 K. As expected, the cell with furthest distance from the cooling plates (i.e. the middle one), shows the highest temperature. Based on the simulations, the authors conclude that the temperature variation impacts oxygen concentration (i.e. dilution due to increased water vaporization at elevated temperature), current density and membrane hydration. In accordance, variations in the performance of the single cells can be detected, as shown in the inset of Figure 16b. Since the cell performance is directly related to temperature, the middle cell shows lowest performance, particularly due to non-uniform oxygen concentration and membrane dehydration. This work highlights the need for proper thermal management to achieve uniform stack temperature distribution. As shown, a valuable tool to probe cooling designs can be modelling. An approach for the improvement of a cooling system can be the variation of the shape (such as U- or Z-shapes of the cooling channels), their dimensions as well as manifold geometries.^[145] Insight in numbers thereof can be found in a recent review.^[149]

As a second method, excess heat can be removed by heat conduction. Here, a thermally conductive material can be inserted between the single cells, acting as heat spreader.^[150] An example for such a material can be pyrolytic graphite sheets.^[151] Besides, heat pipes can act as such a passive cooling system when using a material of high thermal conductivity.^[152,153]

As a last approach, FC stacks can be cooled by air. If not supplied by pure oxygen, cooled, compressed and humidified air is supplied to the cathode as a reactant gas. However, exhaust streams alone only contribute little to the heat removal. Therefore, additional air-cooling can be achieved by passing air through flow channels, e.g., by a fan.^[154,155,156,157] As for the liquid cooling, the design of the flow channels also plays an important role for air-cooling.^[158] Alternatively, reactant supply and cooling circuit can be combined in a so-called 'open-cathode' configuration. Hereby, the PEMFC is allowed to 'breathe in' ambient air that can be supplied to the gas channels with a fan.^[159,160] Smart design of the air flow channels leading to the cathode and channels passing through the cell for cooling can help to achieve a uniform temperature distribution.^[161,162] An example of the temperature distribution in such an open-cathode cell is

given in Figure 16c. The authors applied 3D computational fluid dynamics modeling to predict the temperature distribution, as well as the influence on reactant mass fraction.^[136] The PEMFC was comprised of five MEAs cooled in an open-cathode design, as sketched in the inset of Figure 16c. The temperature distribution was modeled at two different output voltages. The inlet of the cathode was set to a temperature of 300 K and the outside walls to ambient temperatures. In this configuration, maximum temperature variations of ~10 K were observed at lower voltage output, while at higher voltage output lower variations in temperature were detected. The maximum temperature can be monitored in the catalyst layers, due to heat released by the reactions as well as ohmic heating.

In summary, thermal management is an important constituent of a PEMFC. Uniform temperature can be achieved by active cooling with air/ liquid or by inserting a material able to passively take away excess heat via heat conduction. The success of a cooling technique (or their combinations) can either be visualized experimentally (e.g. by thermography) or predicted by modelling (e.g. via computational fluid dynamics).

6. Conclusions and Outlook

In conclusion, we reviewed the impact of temperature on the performance and durability of PEMFCs. In the first part, *in-situ* measurement methods to monitor the temperature distribution along the flow channels and perpendicular to the membrane were addressed. Monitoring heterogeneity in the temperature distribution can help to gain insight on local current densities, relative humidification and water condensation between GDL and BPP. Herein, understanding the mechanisms that determine local temperatures are incremental for stable and durable PEMFC operation. However, little information is given on in-plane temperature distributions during stack operation, which could serve as input for the electrochemical validation of novel fuel cell materials. Accompanying *in-situ* methods, *ex-situ* analysis can be named as a versatile tool to detect compound degradation, often including post-mortem analysis of fuel cell components being operated at realistic temperatures. At low temperatures, the formation of ice, especially within pores and at the layer interfaces, is known to lead to mechanical instabilities. Even though the degradation of GDLs, MPLs, electrodes and the membrane has largely been investigated at these temperatures, little details can be found on the impact of cold starts on the degradation of the BPPs. Nevertheless, post-mortem analysis of cold start effects on coated metallic BPPs might be beneficial, since different thermal expansion coefficients – especially for carbon coated BPPs – might also induce cell failure. Moreover, using post-mortem analysis after high temperature operation, carbon corrosion, chemical and mechanical degradation of the membrane, as well as the BPPs could be visualized. The here presented methods can serve as powerful tool to monitor and localize components prone to failure and help in design of stable fuel cells.

In the second part of this review, material design challenges regarding the degradation of the MEA were discussed. Typical

degradation mechanisms of Pt/C-based CCLs include particle sintering, Pt dissolution and carbon corrosion. Moreover, in the case of Pt alloy nanoparticles used as catalyst, alloy composition and shape are particularly sensitive to the applied temperatures. Promising strategies to mitigate instabilities are the dealloying of the catalyst prior to operation, in order to reduce leaching of the less noble component during fuel cell operation. Besides, introducing structural disorder can be beneficial in terms of durability. The GDLs, usually based on carbon, suffer from mechanical instabilities, especially at sub-zero temperatures due to ice formation. Concerning the proton conducting membrane, temperatures higher than 100 °C can lead to the dry out of widely used Nafion-type polymers. This dry out of the membrane is correlated with mechanical and chemical degradation and, in turn, failure. This can be prevented by chemical modification or by usage of hybrid materials, where metallic or carbon fillers assist in water uptake and increase the overall stability of the membranes. However, long term ASTs operating these membranes at elevated temperatures remain open. The effect of relative humidity on fuel cell operation was discussed. An RH below 60% leads to a poor performance of the ORR. RH values above 60% were found to not improve fuel cell performance anymore but to significantly accelerate degradation of the carbon support. Due to little tolerance of the PEMFC components to temperature fluctuations and excess heat produced during operation, proper thermal management of a PEMFC stack is inevitable. Different approaches can be taken in order to achieve a uniform temperature contribution: active cooling by a liquid coolant or air as well as the insertion of a heat spreader. The uniformity of the temperature can be accessed either experimentally or predicted by mathematical models.

The Department of Energy targets to reach a maximum operational temperature of 120 °C. As described in this review, many degradation mechanisms increase with increasing temperature. Therefore, operation above 100 °C introduces challenges to reach the desired lifetime of fuel cells. When comparing stack operation at 80 and 120 °C, a six-fold increase in voltage degradation can be observed. Membrane degradation due to local humidity fluctuations might be the origin of increased degradation rates. At elevated temperatures, also increased chemical degradation due to radical attack of the membrane might increase degradation rates.

Acknowledgements

We kindly acknowledge the financial support from German Research Foundation (DFG) under Grant No. 355784621, under Germany's Excellence Strategy-EXC 2089/1-390776260, under Germany's Excellence cluster "e-conversion" and DFG projects BA 5795/4-1 and TUM IGSSSE, project 11.01. We also acknowledge the BMW Group, Germany for supporting the research. Open access funding enabled and organized by Projekt DEAL.

Conflict of Interest

The authors declare no conflict of interest.

Keywords: temperature effect · PEMFCs · membrane electrode assembly · gas diffusion layers · membrane degradation

- [1] J. Shin, W.-S. Hwang, H. Choi, *Technological Forecasting and Social Change* **2019**, *143*, 239–248.
- [2] B. Nastasi, *Academic Press, Solar Hydrogen Production* **2019**, 31–44.
- [3] I. Staffell, D. Scamman, A. V. Abad, P. Balcombe, P. E. Dodds, P. Ekins, N. Shah, K. R. Ward, *Energy Environ. Sci.* **2019**, *12*, 463–491.
- [4] A. de Frank Brujin, G. J. M. Janssen, *Springer New York*, **2013**, 249–303.
- [5] J. O. Jensen, D. Aili, Y. Hu, L. N. Cleemann, Q. Li, High-Temperature Polymer Electrolyte Membrane Fuel Cells. In: Nakashima N. (eds) *Nanocarbons for Energy Conversion: Supramolecular Approaches. Nanostructure Science and Technology, Springer International Publishing*, **2019**, 45–79.
- [6] T. Ruij, A. M. Dreizler, J. Mitzel, E. Gülzow, *J. Power Sources* **2016**, *303*, 257–266.
- [7] A. Kraysberg, Y. Ein-Eli, *Energy Fuels* **2014**, *28*, 7303–7330.
- [8] M. Yandrasits, DOE Hydrogen and Fuel Cells Program, *New Fuel Cell Membranes with Improved Durability and Performance*, **2015**.
- [9] R. Alink, D. Gerteisen, M. Oszcipok, *J. Power Sources* **2008**, *182*, 175–187.
- [10] T.-F. Cao, Y.-T. Mu, J. Ding, H. Lin, Y.-L. He, W.-Q. Tao, *Int. J. Heat Mass Transfer* **2015**, *87*, 544–556.
- [11] A. Hakenjos, H. Muentner, U. Wittstadt, C. Hebling, *J. Power Sources* **2004**, *131*, 213–216.
- [12] M. Wang, H. Guo, C. Ma, *J. Power Sources* **2006**, *157*, 181–187.
- [13] Y. Kondo, H. Daiguji, E. Hihara, *The Proceedings of the International Conference on Power Engineering (ICOPE)* **2003**, *2*, 463–468.
- [14] R. Shimoi, M. Masuda, K. Fushinobu, Y. Kozawa, K. Okazaki, *J. Energy Resour. Technol.* **2004**, *126*, 258–261.
- [15] H. Kahraman, M. F. Orhan, *Energy Convers. Manage.* **2017**, *133*, 363–384.
- [16] N. V. Lugeva, S. M. Lugev, A. A. Dunaev, *Phys. Solid State* **2003**, *45*, 449–452.
- [17] O. A. Obeisun, Q. Meyer, E. Engebretsen, D. P. Finegan, J. B. Robinson, G. Hinds, P. R. Shearing, D. J. L. Brett, *Int. J. Hydrogen Energy* **2015**, *40*, 16786–16796.
- [18] H. Guo, M. H. Wang, J. X. Liu, Z. H. Nie, F. Ye, C. F. Ma, *J. Power Sources* **2015**, *273*, 775–783.
- [19] M. Noorkami, J. B. Robinson, Q. Meyer, O. A. Obeisun, E. S. Fraga, T. Reisch, P. R. Shearing, D. J. L. Brett, *Int. J. Hydrogen Energy* **2014**, *39*, 1439–1448.
- [20] F. Nandjou, J.-P. Poirot-Crouvezier, M. Chandesris, J.-F. Blachot, C. Bonnaud, Y. Bultel, *J. Power Sources* **2016**, *326*, 182–192.
- [21] J. B. Robinson, P. R. Shearing, D. J. L. Brett, *Journal of Imaging* **2016**, *2*, 2.
- [22] E. Engebretsen, J. B. Robinson, O. Obeisun, T. Mason, D. Finegan, G. Hinds, P. R. Shearing, D. J. L. Brett, *J. Power Sources* **2016**, *302*, 210–214.
- [23] J. P. Rakotoniaina, O. Breitenstein, M. Langenkamp, *Mater. Sci. Eng. B* **2002**, *91–92*, 481–485.
- [24] J. P. Sabawa, A. S. Bandarenka, *Electrochim. Acta* **2019**, *311*, 21–29.
- [25] L. Rasha, J. I. S. Cho, T. P. Neville, A. Corredera, P. R. Shearing, D. J. L. Brett, *J. Power Sources* **2019**, *440*, 227160.
- [26] H. Wang, A. Gaillard, D. Hissel, *Renewable Energy* **2019**, *141*, 124–138.
- [27] N. Kitamura, K. Manabe, Y. Nonobe, M. Kizaki, *SAE [Tech. Pap.]* **2010**.
- [28] A. Morin, Z. Peng, J. Jestin, M. Detrez, G. Gebel, *Solid State Ionics* **2013**, *252*, 56–61.
- [29] Y. Luo, K. Jiao, *Prog. Energy Combust. Sci.* **2018**, *64*, 29–61.
- [30] P. J. S. Vie, S. Kjelstrup, *Electrochim. Acta* **2004**, *49*, 1069–1077.
- [31] A. Thomas, G. Maranzana, S. Didierjean, J. Dillet, O. Lottin, *J. Electrochem. Soc.* **2013**, *160*, 191–204.
- [32] S. Basu, M. W. Renfro, B. M. Cetegen, *J. Power Sources* **2006**, *162*, 286–293.
- [33] N. A. David, P. M. Wild, J. Jensen, T. Navessin, N. Djilali, *J. Electrochem. Soc.* **2010**, *157*, 1173–1179.
- [34] N. A. David, P. M. Wild, J. Hu, N. Djilali, *J. Power Sources* **2009**, *192*, 376–380.

- [35] K. Inman, X. Wang, B. Sangeorzan, *J. Power Sources* **2010**, *195*, 4753–4757.
- [36] K. Inman, X. Wang, *J. Electrochem. Soc.* **2013**, *160*, 496–500.
- [37] O. Breitenstein, W. Warta, M. C. Schubert, Lock-in Thermography, *In Springer Series in Advanced Microelectronics*, **2018**.
- [38] Q. Yan, H. Toghiani, Y.-W. Lee, K. Liang, H. Causey, *J. Power Sources* **2006**, *160*, 1242–1250.
- [39] Y. Ishikawa, M. Shiozawa, M. Kondo, K. Ito, *Int. J. Heat Mass Transfer* **2014**, *74*, 215–227.
- [40] X. Xie, R. Wang, K. Jiao, G. Zhang, J. Zhou, Q. Du, *Renewable Energy* **2018**, *117*, 125–134.
- [41] Y. Tabe, K. Yamada, R. Ichikawa, Y. Aoyama, K. Suzuki, T. Chikahisa, *J. Electrochem. Soc.* **2016**, *163*, 1139–1145.
- [42] S. Hirakata, M. Hara, K. Kakinuma, M. Uchida, D. A. Tryk, H. Uchida, M. Watanabe, *Electrochim. Acta* **2014**, *120*, 240–247.
- [43] F. Onishi, Y. Tabe, T. Chikahisa, *ECS Trans.*, **2018**, *86*, 89–96.
- [44] H. Wang, J. A. Turner, *Fuel Cells: Data, Facts and Figures*, Wiley-VCH, **2016**, 128–134.
- [45] W. Bi, T. F. Fuller, *J. Electrochem. Soc.* **2008**, *155*, B215–B221.
- [46] S. R. Dhanushkodi, S. Kundu, M. W. Fowler, M. D. Pritzker, *J. Power Sources* **2014**, *245*, 1035–1045.
- [47] W. Bi, G. E. Gray, T. F. Fuller, *Electrochem. Solid-State Lett.*, **2007**, *10*, 101–104.
- [48] J. C. Meier, C. Galeano, I. Katsounaros, J. Witte, H. J. Bongard, A. A. Topalov, C. Baldizzone, S. Mezzavilla, F. Schüth, K. J. J. Mayrhofer, *Beilstein J. Nanotechnol.* **2014**, *5*, 44–67.
- [49] R. L. Borup, J. R. Davey, F. H. Garzon, D. L. Wood, M. A. Inbody, *J. Power Sources* **2006**, *163*, 76–81.
- [50] L. Dubau, F. Maillard, *Electrochem. Commun.* **2016**, *63*, 65–69.
- [51] T. Mittermeier, A. Weiß, F. Hasché, G. Hübner, H. A. Gasteiger, *J. Electrochem. Soc.* **2016**, *164*, F127–F137.
- [52] D. A. Stevens, J. R. Dahn, *Carbon* **2005**, *43*, 179–188.
- [53] L. Castanheira, W. O. Silva, F. H. Lima, A. Crisci, L. Dubau, F. Maillard, *ACS Catal.* **2015**, *5*, 2184–2194.
- [54] S. M. Andersen, M. Borghei, P. Lund, Y. R. Elina, A. Pasanen, E. Kauppinen, V. Ruiz, P. Kauranen, E. M. Skou, *Solid State Ionics* **2013**, *231*, 94–101.
- [55] C. Cremers, T. Jurzinsky, J. Meier, A. Schade, M. Branghofer, K. Pinkwart, J. Tuebke, *J. Electrochem. Soc.* **2018**, *165*, F3307–F3315.
- [56] R. Kunkel, N. Baumann, T. Jurzinsky, C. Cremers, *Fuel Cells* **2019**, *20*, 236–244.
- [57] S. Maldonado, K. J. Stevenson, *J. Phys. Chem. B* **2005**, *109*, 4707–4716.
- [58] C. K. Acharya, C. H. Turner, *J. Phys. Chem. B* **2006**, *110*, 17706–17710.
- [59] A. Pătru, A. Rabis, S. E. Temmel, R. Kotz, T. J. Schmidt, *Catal. Today* **2016**, *262*, 161–169.
- [60] T. Yoshida, K. Kojima, *Electrochem. Soc. Interface* **2015**, *24*, 45–49.
- [61] M. Oezaslan, F. Hasché, P. Strasser, *J. Electrochem. Soc.* **2012**, *159*, B444–B454.
- [62] V. R. Stamenkovic, B. Fowler, B. S. Mun, G. Wang, P. N. Ross, C. A. Lucas, N. M. Marković, *Science* **2007**, *315*, 493–497.
- [63] J. Fichtner, B. Garlyyev, S. Watzel, H. A. El-Sayed, J. Schwämmlein, W. Li, F. Maillard, L. Dubau, J. Michalicka, J. Macak, A. Holleitner, A. S. Bandarenka, *ACS Appl. Mater. Interfaces* **2019**, *11*, 5129–5135.
- [64] C. Song, Y. Tang, J. L. Zhang, J. Zhang, H. Wang, J. Shen, S. McDermid, J. Li, P. Kozak, *Electrochim. Acta* **2007**, *52*, 2552–2561.
- [65] J. J. Baschuk, X. Li, *Int. J. Energy Res.* **2001**, *25*, 695–713.
- [66] S. Chen, H. A. Gasteiger, K. Hayakawa, T. Tadac, Y. Shao-Horn, *J. Electrochem. Soc.* **2010**, *157*, A82–A97.
- [67] A. S. Aricó, A. Stassi, I. Gatto, G. Monforte, E. Passalacqua, V. Antonucci, *J. Phys. Chem. C* **2010**, *114*, 15823–15836.
- [68] A. S. Aricó, A. Stassi, E. Modica, R. Ornelas, I. Gatto, E. Passalacqua, V. Antonucci, *J. Power Sources* **2008**, *178*, 525–536.
- [69] J. Durst, M. Chatenet, F. Maillard, *Phys. Chem. Chem. Phys.* **2012**, *14*, 13000–13009.
- [70] D. D. Papadimas, R. K. Ahluwalia, N. Kariuki, D. Myers, K. L. More, D. A. Cullen, B. T. Sneed, K. C. Neyerlin, R. Mukundan, R. L. Borup, *J. Electrochem. Soc.* **2018**, *165*, F3166–F3177.
- [71] H. Yano, I. Arima, M. Watanabe, A. Iiyama, H. Uchida, *J. Electrochem. Soc.* **2017**, *164*, F966–F972.
- [72] L. Dubau, F. Maillard, M. Chatenet, L. Guetaz, J. André, E. Rossinot, *J. Electrochem. Soc.*, **2010**, *157*, B1887–B1895.
- [73] L. Dubau, M. Lopez-Haro, J. Durst, F. Maillard, *Catal. Today* **2016**, *262*, 146–154.
- [74] I. Dutta, M. K. Carpenter, M. P. Balogh, J. M. Ziegelbauer, T. E. Moylan, M. H. Atwan, N. P. Irish, *J. Phys. Chem. C* **2010**, *114*, 39, 16309–16320.
- [75] F. Hasché, M. Oezaslan, P. Strasser, *J. Electrochem. Soc.* **2012**, *159*, B24–B33.
- [76] L. Gan, S. Rudi, C. Cui, M. Heggen, P. Strasser, *Small* **2016**, *12*, 3189–3196.
- [77] B. Han, C. E. Carlton, A. Kongkanand, R. S. Kukreja, B. R. Theobald, L. Gan, R. O'Malley, P. Strasser, F. T. Wagner, Y. Shao-Horn, *Energy Environ. Sci.* **2015**, *8*, 258–266.
- [78] C. Chen, Y. Kang, Z. Huo, Z. Zhu, W. Huang, H. L. Xin, J. D. Snyder, D. Li, J. A. Herron, M. Mavrikakis, M. Chi, K. L. More, Y. Li, N. M. Markovic, G. A. Somorjai, P. Yang, V. R. Stamenkovic, *Science* **2014**, *343*, 1339–1343.
- [79] L. Dubau, T. Asset, R. Chattot, C. Bonnaud, V. Vanpeene, J. Nelayah, F. Maillard, *ACS Catal.* **2015**, *5*, 5333–5341.
- [80] M. Li, Z. Zhao, T. Cheng, A. Fortunelli, C.-Y. Chen, R. Yu, Q. Zhang, L. Gu, B. V. Merinov, Z. Lin, E. Zhu, T. Yu, Q. Jia, J. Guo, L. Zhang, W. A. Goddard III, Y. Huang, X. Duan, *Science* **2016**, *354*, 1414–1419.
- [81] R. Chattot, O. Le Bacq, V. Beermann, S. Kühl, J. Herranz, S. Henning, L. Kühn, T. Asset, L. Guétaz, G. Renou, J. Drnec, P. Bordet, A. Pasturel, A. Eychmüller, T. J. Schmidt, P. Strasser, L. Dubau, F. Maillard, *Nat. Mater.* **2018**, *17*, 827–833.
- [82] Q. Meyer, Y. Zeng, C. Zhao, *Adv. Mater.* **2019**, *31*, 1901900.
- [83] J. Park, H. Oh, T. Ha, Y. I. Lee, K. Min, *Appl. Energy* **2015**, *155*, 866–880.
- [84] A. Forner-Cuenca, J. Biesdorf, L. Gubler, P. M. Kristiansen, T. J. Schmidt, P. Boillat, *Adv. Mater.* **2015**, *27*, 6317–6322.
- [85] S. Park, J. W. Lee, B. N. Popov, *J. Hydrogen Energy* **2012**, *37*, 5850–5865.
- [86] P. Irmischer, D. Qui, H. Janßen, W. Lehnert, D. Stolten, *J. Hydrogen Energy* **2019**, *44*, 23406–23415.
- [87] J. Wu, X. Z. Yuan, J. J. Martin, H. Wang, J. Zhang, J. Shen, S. Wu, W. Merid, *J. Power Sources* **2008**, *184*, 104–119.
- [88] R. W. Atkinson, Y. Garsany, B. D. Gould, K. E. Swider-Lyons, I. V. Zenyuk, *ACS Appl. Energy Mater.*, **2018**, *1*, 191–201.
- [89] R. Omrani, B. Shabani, *Int. J. Hydrogen Energy* **2017**, *42*, 28515–28536.
- [90] S. J. Lim, G.-G. Park, J.-S. Park, Y.-J. Sohn, S.-D. Yim, T.-H. Yang, B. K. Hong, C.-S. Kim, *Int. J. Hydrogen Energy* **2010**, *35*, 13111–13117.
- [91] Y. Chen, C. Jiang, C. Cho, *Polymer* **2019**, *11*, 428.
- [92] P. Shrestha, R. Banerjee, J. Lee, N. Ge, D. Muirhead, H. Liu, A. K. C. Wong, D. Ouellette, B. Zhao, A. Bazyak, *J. Power Sources* **2018**, *402*, 468–482.
- [93] H. Liu, M. G. George, N. Ge, D. Muirhead, P. Shrestha, J. Lee, R. Banerjee, R. Zeis, M. Messerschmidt, J. Scholta, P. Krolla, *J. Electrochem. Soc.* **2018**, *165*, F3271–F3280.
- [94] F. I. Allen, L. R. Comolli, A. Kusoglu, M. A. Modestino, A. M. Minor, A. Z. Weber, *ACS Macro Lett.* **2015**, *4*, 1–5.
- [95] M. Feng, R. Qu, Z. Wei, L. Wang, P. Sun, Z. Wang, *Sci. Rep.* **2015**, *5*, 9859–9867.
- [96] A. Kusoglu, A. Z. Weber, *Chem. Rev.* **2017**, *117*, 987–1104.
- [97] W. Schmittinger, A. Vahidi, *J. Power Sources* **2008**, *180*, 1–14.
- [98] Q. Li, D. Aili, H. A. Hjuler, J. O. Jensen, *High Temperature Polymer Electrolyte Membrane Fuel Cells*, Springer Switzerland, **2016**.
- [99] L. Ghassemzadeh, S. Holdcroft, *J. Am. Chem. Soc.* **2013**, *135*, 8181–8184.
- [100] S. Kreitmeier, M. Michiardi, A. Wokaun, F. N. Buchi, *Electrochim. Acta* **2012**, *80*, 240–247.
- [101] K. D. Kreuer, M. Schuster, B. Obliers, O. Diat, U. Traub, A. Fuchs, U. Klock, S. J. Paddison, J. Maier, *J. Power Sources* **2008**, *178*, 499–509.
- [102] A. Kusoglu, T. J. Dursch, A. Z. Weber, *Adv. Funct. Mater.* **2016**, *26*, 4961–4975.
- [103] S. Slade, J. Smith, S. Campbell, T. Ralph, C. P. de Leon, F. Walsh, *Electrochim. Acta* **2010**, *55*, 6818–6829.
- [104] M. Amjadi, S. Rowshanzamir, S. J. Peighambaroust, M. G. Hosseini, M. H. Eikani, *Int. J. Hydrogen Energy* **2010**, *35*, 9252–9260.
- [105] M. K. Mistry, N. R. Choudhury, N. K. Dutta, R. Knott, Z. Shi, S. Holdcroft, *Chem. Mater.* **2008**, *20*, 6857–6870.
- [106] Y. Devrim, *J. Appl. Polym. Sci.* **2014**, *131*, 40541–40541.
- [107] Y. Zhai, H. Zhang, J. Hu, B. Yi, *J. Membr. Sci.* **2006**, *280*, 148–155.
- [108] L. L. Mao, A. K. Mishra, N. H. Kim, J. H. Lee, *J. Membr. Sci.* **2012**, *411*, 91–98.
- [109] P. Trogasdas, J. Parrondo, V. Ramani, *ACS Appl. Mater. Interfaces* **2012**, *4*, 5098–5102.
- [110] S. Y. So, S. C. Kim, S. Y. Lee, *J. Membr. Sci.* **2010**, *360*, 2010–2016.
- [111] J. Yin, *J. Phys. Chem. C* **2018**, *122*, 9710–9717.
- [112] W. F. Chen, J. S. Wu, P. L. Kuo, *Chem. Mater.* **2008**, *20*, 5756–5767.
- [113] R. Kannan, B. A. Kakade, V. K. Pillai, *Angew. Chem. Int. Ed.* **2008**, *47*, 2653–2656; *Angew. Chem.* **2008**, *120*, 2693–2696.

- [114] M. S. Asgari, M. Nikazar, P. Molla-abbasi, M. M. Hasani-Sadrabadi, *Int. J. Hydrogen Energy* **2013**, *38*, 5894–5902.
- [115] A. Chandan, M. Hattenberger, A. El-kharouf, S. Du, A. Dhir, V. Self, B. G. Pollet, A. Ingram, W. Bujalski, *J. Power Sources* **2013**, *231*, 264–278.
- [116] D. W. Shin, M. D. Guiver, Y. M. Lee, *Chem. Rev.* **2017**, *117*, 4759–4805.
- [117] Q. Yan, H. Toghiani, J. Wu, *J. Power Sources* **2006**, *158*, 316–325.
- [118] S. Chugh, C. Chaudhari, K. Sonkar, A. Sharma, G. S. Kapur, S. Ramakumar, *Int. J. Hydrogen Energy* **2020**, *45*, 8866–8874.
- [119] D. N. Ozen, B. Timurkutluk, K. Altinisik, *Renewable Sustainable Energy Rev.* **2016**, *59*, 1298–1306.
- [120] A. Sveshnikova, K. Abrosimov, A. Khayrullina, A. Ustinov, *J. Renewable Sustainable Energy* **2017**, *9*, 044301.
- [121] A. Sveshnikova, G. Di Marcoberardino, C. Pirrone, A. Bischi, G. Valenti, A. Ustinov, S. Campanari, *Energy Procedia* **2017**, *142*, 1661–1667.
- [122] X.-D. Wang, Y.-Y. Duan, W.-M. Yan, F.-B. Weng, *J. Power Sources* **2008**, *176*, 247–258.
- [123] K. N. Neyerlin, H. A. Gasteiger, C. K. Mittelsteadt, J. Jorne, W. Gu, *J. Electrochem. Soc.* **2005**, *152*, A1073.
- [124] H. Xu, Y. Song, H. R. Kunz, J. M. Fenton, *J. Electrochem. Soc.* **2005**, *152*, A1828.
- [125] Y. Liu, M. W. Murphy, D. R. Baker, W. Gu, C. Ji, J. Jorne, H. A. Gasteiger, *J. Electrochem. Soc.* **2009**, *156*, B970.
- [126] F. A. Uribe, *J. Electrochem. Soc.* **1992**, *139*, 765.
- [127] C. A. Reiser, L. Bregoli, T. W. Patterson, J. S. Yi, J. D. Yang, M. L. Perry, T. D. Jarvi, *Electrochem. Solid-State Lett.* **2005**, *8*, A273.
- [128] K. H. Lim, H.-S. Oh, S.-E. Jang, Y.-J. Ko, H.-J. Kim, H. Kim, *J. Power Sources* **2009**, *193*, 575–579.
- [129] S. Kreitmeier, A. Wokaun, F. N. Büchi, *J. Electrochem. Soc.* **2012**, *159*, F787–F793.
- [130] A. Ofstad, J. Davey, S. Sunde, R. L. Borup, *ECS Trans.* **2008**, *16*, 1301–1311.
- [131] T. Mittermeier, A. Weiß, F. Hasché, H. A. Gasteiger, *J. Electrochem. Soc.* **2018**, *165*, F1349–F1357.
- [132] Y. Wang, X. Zhang, Q. Feng, J. Zou, C. Zhou, L. Zeng, J. Fan, H. Zhao, H. Huang, H. Fu, H. Li, H. Wang, *Int. J. Green Energy* **2020**, *17*, 157–170.
- [133] J. Zhang, Y. Tang, C. Song, J. Zhang, *J. Power Sources* **2007**, *172*, 163–171.
- [134] H. K. Esfeh, M. K. A. Hamid, *Energy Procedia* **2014**, *61*, 2617–2620.
- [135] G. Zhang, H. Yuan, Y. Wang, K. Jiao, *Appl. Energy* **2019**, *255*, 113865–113875.
- [136] J. Macedo-Valencia, J. M. Sierra, S. J. Figueroa-Ramírez, S. E. Díaz, M. Meza, *Int. J. Hydrogen Energy* **2016**, *41*, 23425–23433.
- [137] M. Ramezanizadeh, M. A. Nazari, M. H. Ahmadi, L. Chen, *Int. J. Heat Mass Transfer* **2019**, *139*, 517–525.
- [138] G. Zhang, S. G. Kandlikar, *Int. J. Hydrogen Energy* **2012**, *37*, 2412–29.
- [139] A. Faghri, Z. Guo, *Int. J. Heat Mass Transfer* **2005**, *48*, 3891–3920.
- [140] G. Zhang, K. Jiao, *J. Power Sources* **2018**, *391*, 120–133.
- [141] J. Clement, X. Wang, *Appl. Therm. Eng.* **2013**, *50*, 268–274.
- [142] M. H. Ahmadi, A. Mirlohi, M. Alhuyi Nazari, R. Ghasempour, *J. Mol. Liq.* **2018**, *265*, 181–188.
- [143] J. Park, X. Li, *J. Power Sources* **2006**, *162*, 444–459.
- [144] R. M. Aslam, D. B. Ingham, M. S. Ismail, K. J. Hughes, L. Ma, M. Pourkashanian, *J. Energy Inst.* **2019**, *92*, 311–318.
- [145] A. Amirfazli, S. Asghari, M. Sarraf, *Energy* **2018**, *145*, 141–151.
- [146] J. G. Pharoah, O. S. Burheim, *J. Power Sources* **2010**, *195*, 5235–5245.
- [147] E. Afshari, M. Ziaei-Rad, M. M. Dehkordi, *J. Energy Inst.* **2017**, *90*, 752–763.
- [148] Y. Saygili, I. Eroglu, S. Kincal, *Int. J. Hydrogen Energy* **2015**, *40*, 615–622.
- [149] Y. Wang, D. F. R. Diaz, K. S. Chen, Z. Wang, X. C. Adroher, *Mater. Today* **2020**, *32*, 178–203.
- [150] M. R. Hajmohammadi, M. Ahmadian, S. S. Nourazar, *Int. J. Mech. Sci.* **2019**, *150*, 420–426.
- [151] C.-Y. Wen, Y.-S. Lin, C.-H. Lu, T.-W. Luo, *Int. J. Hydrogen Energy* **2011**, *36*, 6082–6089.
- [152] M. V. Oro, E. Bazzo, *Appl. Therm. Eng.* **2015**, *90*, 848–857.
- [153] N. Shirzadi, R. Roshandel, M. B. Shafii, *Heat Transfer Eng.* **2017**, *38*, 1595–1605.
- [154] R. Atan, W. A. Najmi, *Procedia Eng.* **2012**, *41*, 1735–1742.
- [155] K. P. Adzakpa, J. Ramousse, Y. Dubé, H. Akremi, K. Agbossou, M. Dostie, A. Poulin, M. Fournier, *J. Power Sources* **2008**, *179*, 164–176.
- [156] A. De las Heras, F. J. Vivas, F. Segura, M. J. Redondo, J. M. Andújar, *Renewable Energy* **2018**, *125*, 1–20.
- [157] L. Luo, Q. Jian, B. Huang, Z. Huang, J. Zhao, S. Cao, *Renewable Energy* **2019**, *143*, 1067–1078.
- [158] M. Ghasemi, A. Ramiar, A. A. Ranjbar, S. M. Rahgoshay, *Int. J. Hydrogen Energy* **2017**, *42*, 24319–24337.
- [159] A. P. Sasmito, K. W. Lum, E. Birgersson, A. S. Mujumdar, *J. Power Sources* **2010**, *195*, 5550–5563.
- [160] C. Y. Ling, H. Cao, Y. Chen, M. Han, E. Birgersson, *Appl. Energy* **2016**, *164*, 670–675.
- [161] J. Lee, M. H. Gundu, N. Lee, K. Lim, S. W. Lee, S. S. Jang, J. Y. Kim, H. Ju, *Int. J. Hydrogen Energy* **2019**, *45*, 11704–11713.
- [162] W.-M. Yan, M.-S. Zeng, T.-F. Yang, C.-Y. Chen, M. Amani, P. Amani, *Int. J. Hydrogen Energy* **2019**, doi.org/10.1016/j.ijhydene.2019.08.146.

Manuscript received: April 24, 2020

Accepted manuscript online: June 5, 2020